Biogenic isoprene emissions driven by regional weather predictions using different initialization methods: Case studies during the SEAC[4]RS and DISCOVER-AQ airborne campaigns

Min Huang[1,2], Gregory R. Carmichael[3], James H. Crawford[4], Armin Wisthaler[5,6], Xiwu Zhan[7],
Christopher R. Hain[2,a], Pius Lee[8], Alex B. Guenther[9]

[1]George Mason University, Fairfax, VA, USA
[2]University of Maryland, College Park, MD, USA
[3]University of Iowa, Iowa City, IA, USA
[4]NASA Langley Research Center, Hampton, VA, USA
[5]University of Oslo, Oslo, Norway
[6]University of Innsbruck, Innsbruck, Austria
[7]NOAA National Environmental Satellite, Data, and Information Service, College Park, MD, USA
[8]NOAA Air Resources Laboratory, College Park, MD, USA
[9]University of California, Irvine, CA, USA
[a]Now at: NASA Marshall Space Flight Center, Huntsville, AL, USA

Correspondence to: Min Huang (mhuang10@gmu.edu)

Abstract. Land and atmospheric initial conditions of the Weather Research and Forecasting (WRF) model are often interpolated from a different model output. We perform case studies during NASA's SEAC[4]RS and DISCOVER-AQ Houston airborne campaigns, demonstrating that using land initial conditions directly downscaled from a coarser resolution dataset led to significant positive biases in the coupled NASA-Unified WRF (NUWRF, version 7) (near-) surface air temperature and planetary boundary layer height (PBLH) around the Missouri Ozarks and Houston, Texas, as well as poorly partitioned latent and sensible heat fluxes. Replacing land initial conditions with the output from a long-term offline Land Information System (LIS) simulation can effectively reduce the positive biases in NUWRF surface air temperature by ~2°C. We also show that the LIS land initialization can modify surface air temperature errors almost ten times as effectively as applying a different atmospheric initialization method. The LIS-NUWRF based isoprene emission calculations by the Model of Emissions of Gases and Aerosols from Nature (MEGAN, version 2.1) are at least 20% lower than those computed using the coarser resolution data-initialized NUWRF run, and are closer to aircraft observation-derived emissions. Higher resolution MEGAN calculations are prone to amplified discrepancies with aircraft observation-derived emissions on small scales. This is possibly resulting from some limitations of MEGAN's parameterization, uncertainty in its inputs on small scale, as well as the representation error and neglecting horizontal transport in deriving emissions from aircraft data. This study emphasizes the importance of proper land initialization to the coupled atmospheric weather modeling and the follow-on emission modeling. We anticipate it to be also critical to accurately representing other processes included in air quality modeling and chemical data assimilation. Having more confidence in the weather inputs is also beneficial for determining and quantifying the other sources of uncertainties (e.g., parameterization, other input data) of the models that they drive.

1

1 Introduction

The weather-dependent emissions of biogenic volatile organic compounds (BVOCs), including the highly reactive species isoprene (C_5H_8), contribute to the formation of secondary short-lived climate pollutants such as ozone (O_3) and secondary organic aerosol. Therefore, these emissions affect air quality on local, regional, and global scales, which feed back to the climate. For example, a modeling study by Li et al. (2007) showed that a 50% reduction in Houston isoprene emissions led to 5-25 ppbv summertime afternoon O_3 reductions at its urban areas, and the transport of isoprene from north of the urban Houston area had non-negligible impact on its isoprene budget within several days. Summertime isoprene emitted from the Missouri Ozarks (also known as "isoprene volcano", where a high density of oak trees efficiently emit isoprene), along with its oxidation product formaldehyde (HCHO), can be transported to urban areas (e.g., Chicago and St. Louis) and affect their O_3 burdens (Wiedinmyer et al., 2005). Ozone and peroxyacetyl nitrate produced from isoprene and other O_3 precursors can also affect air quality on hemispheric scale. Fiore et al. (2011) compared the O_3 sensitivity to a 20% change in North American (NA) isoprene emissions with the sensitivity to a 20% change in NA anthropogenic emissions. Over NA, the former was ~1/3 of the latter, and over Europe and North Africa, the former was more than half of the latter in summer and fall. Therefore, possible increases in future isoprene emissions due to land cover and climate change may offset the surface O_3 decreases due to controlling anthropogenic emissions in NA and its downwind continents.

The Model of Emissions of Gases and Aerosols from Nature (MEGAN, Guenther et al., 2006, 2012) has been frequently used to generate BVOC emissions on flexible scales for air quality modeling. MEGAN computes emissions based on emission source types and their densities, ambient carbon dioxide (CO_2) concentrations, and meteorological conditions (e.g., temperature, solar radiation, and moisture). It has been found that the MEGAN emissions are often higher than those calculated using other emission models, and are possibly associated with positive biases (e.g., Millet et al., 2008; Warneke et al., 2010; Carlton and Baker, 2011; Canty et al., 2015; Hogrefe et al., 2011; Emmerson et al., 2016). These biases, which still need careful validation with observation-based emission fluxes, can pose significant difficulties to accurately simulating isoprene and secondary air pollutants by chemical transport models. In addition to the impact of MEGAN parameterization, outdated/unrealistic land cover input data and uncertainties of the meteorological inputs are important causes of these biases (e.g., Guenther et al., 2006, 2012; Carlton and Baker, 2011). The positive biases in surface air temperature and radiation fields from meteorological models have been identified as major sources of uncertainty, and certain solutions have been established to reduce the biases such as substituting the modeled radiation with satellite radiation products. Much less has been done at multiple spatial-temporal scales to explore the biases imported from the modeled soil moisture fields although satellite observations have suggested negative correlations between BVOC emissions and soil moisture (e.g., Duncan et al., 2009). MEGAN sensitivity calculations by Sindelarova et al. (2014) showed weak direct impact of soil moisture on the isoprene emissions over vegetated and moist surfaces. However, the variability in soil moisture can indirectly impact BVOCs emissions and their atmospheric distributions through affecting air/canopy temperature and planetary boundary

layer height (PBLH), the key factors controlling isoprene emissions and satellite column measurements (e.g., Palmer et al., 2003; Duncan et al., 2009), especially over the US transitional climate zones including the Great Plains and some east Asian regions (e.g., Miralles et al., 2012; Zeng et al., 2014; Lee et al., 2016; Zaitchik et al., 2012 and the references therein). Therefore, accurately simulating land states and correct representation of land-atmosphere interactions by meteorological models can provide improved inputs for the MEGAN emission calculations.

The performance of coupled land-atmospheric modeling relies on numerous factors such as the choice of land surface model (LSM), nudging methods, and land use/land cover input data (e.g., Jin et al., 2010; Byun et al., 2011; Huang et al., 2016). The initialization of soil moisture and other land fields have also been shown important to the modeled atmospheric weather states (e.g., air temperature, humidity, winds, precipitation, and PBLH) and latent/sensible heat fluxes. Suitable and sufficient LSM spin-up as well as land data assimilation can benefit land surface modeling and the coupled atmospheric weather prediction (e.g., Rodell et al., 2005; Case et al., 2008; 2011; Zeng et al., 2014; Angevine et al., 2014; Collow et al., 2014; Lin and Cheng, 2015; Santanello et al., 2013, 2016). However, potential benefit of appropriate land initialization of numerical weather models to emission and air quality related studies needs to be better understood.

In this study, we performed a number of NASA-Unified Weather Research and Forecasting (NUWRF) sensitivity simulations, in which different land and atmospheric initialization methods and model grid resolutions were tested. The simulated weather states, especially the key variables impacting isoprene emissions such as surface air temperature and radiation, as well as heat fluxes were evaluated against in-situ and remote sensing observations. Isoprene emissions were then calculated by MEGAN, driven by these various NUWRF simulations, and these emission estimates were compared with the aircraft observation-derived during two NASA airborne campaigns in September 2013. The paper is structured as follows: We will first introduce the isoprene emissions calculated by MEGAN (Section 2.1) and observations (Section 2.2), followed by model evaluation datasets (Section 2.3). The NUWRF performance and its impact on isoprene emission estimates will be shown on a specific day in September 2013 (Section 3.1), as well as for multiple days in that month when research flights were executed for an airborne campaign. We will also show extended analyses on interannual variability of drought and vegetation conditions in relation to isoprene emissions during 2005-2014 (Section 3.2). The sources of uncertainty of the emissions will be summarized (Section 3.3) before the conclusions and suggestions on future directions are given in Section 4.

2 Methods and data

2.1 Bottom-up emission calculations

2.1.1 MEGAN model version 2.1

The most recent version of MEGAN (version 2.1, Guenther et al., 2012) generates the net primary biogenic emissions that escape into the atmosphere, i.e., these are only emissions from the canopy to the atmosphere and do not include the chemical fluxes from the atmosphere into the canopy, which on average can be a few percent of the net primary emissions (Guenther et al., 2012). The emissions are estimated based on Equation (1):

$$\text{Emission} = [\varepsilon][\gamma][\rho] \tag{1}$$

where $[\varepsilon]$ stands for the emission factor at standard conditions, $[\rho]$ accounts for the production and loss within the plant canopies, assumed to be 1.0. $[\gamma]$ is a unitless emission activity factor, a product of multiple factors that account for the emission response to light (γ_P), temperature (γ_T), soil moisture (γ_{SM}), leaf age (γ_A), leaf area index (LAI), as well as CO_2 inhibition (γ_{CO2}), the process that reduces isoprene emissions when ambient CO_2 concentration increases above the level of 400 ppmv. Among the meteorological variables, MEGAN emissions are strongly sensitive to radiation and air temperature (Guenther et al., 2012, and the references therein), but less sensitive to soil moisture over vegetated and moist surfaces including the central/southeastern US (Sindelarova et al., 2014), where root zone soil moisture is usually larger than a threshold (the sum of a small empirical value and the soil type-dependent wilting point) above which γ_{SM}=1.0.

The stand-alone version of MEGAN 2.1 was used in this study, which requires the users to provide meteorological and land cover inputs. The land cover and meteorological inputs we used in this study will be introduced in detail in Sections 2.1.2 and 2.1.3, respectively. We ignored the CO_2 impacts on the emissions (i.e., γ_{CO2} = 1.0), as September 2013 CO_2 in-situ measurements at the Mauna Loa, Hawaii Observatory are nearly 400 ppmv (i.e., weekly averages within 393.22-393.53 ppmv, http://scrippsco2.ucsd.edu/assets/data/atmospheric/stations/in_situ_co2/weekly/weekly_in_situ_co2_mlo.csv). Sensitivity calculation by Sindelarova et al. (2014) showed that for the year of 2003, the inclusion of CO_2 impact resulted in a 2.7% increase in MEGAN emissions globally under the 373.1237 ppmv CO_2 environment, corresponding to a γ_{CO2} of 1.0277. Therefore, omitting the CO_2 impacts in this study would not introduce large biases. The γ_{SM} value was also 1.0, as the root zone soil moisture from our meteorological input exceeded the sum of the empirical value and the wilting point (from Chen and Dudhia, 2001) over the regions of interest.

2.1.2 Plant functional type (PFT) and LAI input data

The recommended high-resolution 30 arc-second PFT input files for the year of 2008 (Guenther et al., 2012; http://lar.wsu.edu/megan/docs/NorthAmericaPlantFunction/), based on the Community Land Model 16 PFT classification system, were interpolated to the NUWRF model grids for use in this study. The LAI input was based on the Terra-Moderate

Resolution Imaging Spectroradiometer (MODIS) 8-day product, and the grids with missing data were filled with the monthly-mean MODIS product.

2.1.3 NUWRF meteorological simulations using different land and atmospheric initialization methods

The MEGAN emission calculations in this study were driven by the meteorological fields simulated by the NUWRF (Peters-Lidard et al., 2015) modeling system version 7. The WRF component within this version of NUWRF was modified from the core WRF version 3.5.1, and it simulates atmospheric processes on a terrain-following mass vertical coordinate system over flexible spatial and temporal scales (Skamarock et al., 2008). NUWRF supports coupling between WRF and NASA's Land Information System (LIS), a flexible land surface modeling and data assimilation framework developed to integrate satellite and ground observations and advanced land surface modeling techniques to produce optimal fields of land surface states and fluxes (Kumar et al., 2006, 2008). This coupled system enables the investigation of land-air interactions including evaluating the impact of land initialization and land data assimilation on atmospheric states (e.g., Santanello et al., 2016).

A number of NUWRF meteorological simulations (Table 1) were performed over the contiguous US (CONUS) for September 2013 on 12 km (479×399 grids) and 4 km (1248×900 grids) horizontal resolution Lambert conformal grids that are both centered at 40°N/95°W. As in Huang et al. (2016), the vertical grid spacing recommended by the Texas Commission on Environmental Quality (TCEQ) was implemented. We applied the Noah LSM (Chen and Dudhia, 2001), which contains four soil layers of 0.1, 0.3, 0.6, 1.0 m thicknesses, and is an option widely used in scientific and operational applications (e.g., Ek et al., 2003; Santanello et al., 2016). The Noah LSM is based on grid-dominant land use/land cover types and we chose to use the recommended International Geosphere-Biosphere Programme-modified MODIS 20-category land use/land cover (Figure S1, upper), which reflect more recent conditions than the other available options (Tao et al., 2013; Yu et al., 2012). The commonly-used Mellor-Yamada-Janjic PBL scheme (Janjic, 2002) and the matching Monin-Obukhov (Janjic Eta) surface layer scheme (Monin and Obukhov, 1954) were chosen, although these might lead to shallower, cooler PBL and less vertical mixing than other available schemes in WRF (e.g., Saide et al., 2011; Angevine et al., 2012; Huang et al., 2013; Zhang, Y. et al., 2016). Other key physics options include: the Eta microphysics (Rogers et al., 2001), the Rapid Radiative Transfer Model short- and long-wave radiation (Iacono et al., 2008), and the Betts-Miller-Janjic cumulus parameterization (Janjic, 2000). These simulations were started at 06 UTC (00 Central US Standard Time) of each day. The 4 km and 12 km calculations used 4s and 24s time steps, respectively, and they were recorded hourly at 00:00 (minute:second) for 24 and 48 hours, respectively. The effect of simulation length (i.e., day 1- and day 2- forecasts, defined as the simulations 00-24h and 25-48h since the initial time, respectively) on the 12 km NUWRF performance will be included in the discussion.

As illustrated in Figure 1, we performed three types of NUWRF simulations to evaluate the impact of two land initialization methods (points a and b below, and Figures 1a-b, focus of this study), and two atmospheric initialization methods (points b and c below, and Figures 1b-c):

a) A usual method applied to the 12 km NUWRF grid, in which the atmospheric and land initial conditions (IC) were downscaled from the output of a coarser model North American Regional Reanalysis (NARR, at 32 km horizontal resolution with a 3-hourly time interval, Mesinger et al., 2006). NUWRF atmospheric lateral boundary conditions (LBC) were also downscaled from NARR. NARR is known to be generally drier and warmer than the observations (e.g., Royer and Poirier, 2010; Kennedy et al., 2011). As in default and many WRF simulations, the green vegetation fraction (GVF) input data in this case were based on climatological monthly mean satellite normalized difference vegetation index (NDVI). In previous studies, realistic vegetation density in LSMs has been shown important to accurately represent the partitioning of soil evaporation and canopy transpiration (e.g., Bell et al., 2012). However, in this study, the model did not show considerable sensitivities in response to replacing the climatological monthly GVF with satellite near real-time GVF over this study's focus regions, and these will be briefly discussed in Section 3.1.1;

b) The 12 km and 4 km "control (ctrl) simulations": Same as a), except that NUWRF land IC were instead from the output of long-term (i.e., cold-started from 01 January, 2001, cycled twenty times from 01 January, 2001 to 31 December, 2001 before running all the way through September 2013) offline LIS simulation that allowed land conditions to reach thermodynamical/water equilibrium. The LIS offline spin-up was completed on the same horizontal resolutions as NUWRF, forced by highly resolved atmospheric fields from the Global Data Assimilation System (GDAS) and precipitation data from the Global Land Data Assimilation System (GLDAS). The daily near real-time satellite GVF were used within LIS and NUWRF. "Control" was chosen to name these simulations, consistent with the usage in hydrological modeling and data assimilation communities (e.g., Hain et al., 2012);

c) Two additional 12 km and 4 km "ctrl" simulations: Same as b), except that NUWRF IC and LBC in these simulations were taken from the atmospheric fields of the North American Mesoscale Forecast System (NAM, at 12 km horizontal resolution with a 6-hourly time interval, Janjic, 2003; Janjic et al., 2004), which is known to usually have positive biases in temperature, moisture, and wind speed in the CONUS (e.g., McQueen et al., 2015a, b).

2.2 Emissions derived from in-situ isoprene measurements

The mixed-PBL approach introduced by Warneke et al. (2010) was adopted to derive isoprene emissions during two NASA airborne campaigns in September 2013, which were compared with NUWRF-MEGAN bottom-up emissions. The mixed-PBL approach accounts for isoprene's atmospheric lifetime but neglects the impact of horizontal advection, and it estimates isoprene emissions based on Equation (2):

$$\text{Emission}_{\text{isoprene}} - F_e = [\text{isoprene}] \times \text{boundary layer height} \times k_{\text{OH}} \times [\text{OH}] \tag{2}$$

where [isoprene] and [OH] are the concentrations of isoprene and hydroxyl radical (OH), respectively, and the data used in our calculations will be introduced in Sections 2.2.1-2.2.2; k_{OH} refers to the rate coefficients of isoprene with OH which was set to be 1.01×10^{-10} cm^3/molecule/s; and F_e represents the entrainment flux from the boundary layer to the free troposphere, set constantly to be 30% of the emission flux, based on aircraft isoprene flux measurements over the Amazonian rain forest

5   (Karl et al., 2007). Our NUWRF modeled PBLHs, after being qualitatively evaluated with the aircraft measurements, were used in the emission calculations. The uncertainty of the isoprene emissions derived by this approach will be further discussed in Section 3.3.

2.2.1 Isoprene measurements

NASA's Studies of Emissions and Atmospheric Composition, Clouds and Climate Coupling by Regional Surveys

10   (SEAC[4]RS, Toon et al., 2016, https://espo.nasa.gov/home/seac4rs/content/SEAC4RS) was conducted in August-September 2013. More than 20 research flights were executed, including ten September DC-8 flights over the southeastern US primarily focusing on the attribution and the quantification of trace gas pollution and their distributions as a result of deep convection. In-situ isoprene data measured by the Proton Transfer Reaction-Mass Spectrometry (PTR-MS, de Gouw and Warneke, 2007) on board the DC-8 aircraft were used in the emission calculations.

15

We used data obtained in the Missouri Ozarks ("isoprene volcano") region where biogenic isoprene emissions were high and the potential measurement interferences from furan and 2,3,2-methylbutenol (232-MBO) were negligible: Furan is found in significant concentrations only in biomass burning plumes and no enhancement in the biomass burning tracer acetonitrile was observed in our case studies (details in Section 3.1). 232-MBO is only emitted from the coniferous ecosystems in the

20   western US. These isoprene observation data have an accuracy of ±5%.

Nine research flights were executed in September 2013 (i.e., on 4, 6, 11, 12, 13, 14, 24, 25, 26 of this month) to support the Houston portion of the NASA DISCOVER-AQ (Deriving Information on Surface conditions from Column and Vertically Resolved Observations Relevant to Air Quality, Crawford et al., 2014, https://discover-aq.larc.nasa.gov) field experiment.

25   High-resolution in-situ isoprene measurements during DISCOVER-AQ were made using a proton-transfer-reaction time-of-flight mass spectrometry instrument (PTR-ToF-MS, with an accuracy of ±10%, Müller et al., 2014) on board the P-3B aircraft over selected locations in the Greater Houston area three times a day (i.e., morning, noon-early afternoon, and mid-afternoon) to explore their spatial and diurnal variability. Isoprene measurements from the PTR-ToF-MS are possibly interfered by other VOCs from anthropogenic sources in Houston (e.g., from oil and gas industries). Therefore, we focus on

30   deriving biogenic emissions at the Conroe site, a region north of downtown Houston area with medium vegetation coverage and less strongly influenced by urban transportation/industrial sources and biomass burning plumes (details in Section 3.1). Additionally, we investigated the hourly surface isoprene measurements available at eight TCEQ Automated Gas Chromatograph (AutoGC) monitoring stations, mostly located in the downtown Houston area. The data before sunrise and

after sunset, when biogenic isoprene emissions are at their daily minima, are particularly useful for determining the regional background and non-biogenic isoprene levels, and therefore they helped quantify the uncertainty in the observation-derived emissions. The Limit of Detection applied to all AutoGC target compounds is currently 0.4 ppbC (0.08 ppbv for isoprene).

The ground speed of the DC-8 and P-3B aircraft was around 8-9 km/minute near the "isoprene volcano" areas during SEAC[4]RS and 9-14 km/minute at around Conroe during DISCOVER-AQ within the focused time period. Therefore, the aircraft data averaged in 1-minute interval (released on 10 February, 2016 and 23 July, 2015 for SEAC[4]RS and DISCOVER-AQ, respectively) were used to estimate the emissions, as they represent isoprene concentrations on similar spatial scales to NUWRF-MEGAN. At around Conroe, multiple P-3B aircraft data points correspond to several NUWRF model grids, and the averaged emissions based on NUWRF-MEGAN and the median PBL observations were used in the comparisons.

2.2.2 OH from the NOAA National Air Quality Forecasting Capability (NAQFC)

Due to the lack of aircraft OH measurements in September 2013, the OH concentrations simulated by the NOAA NAQFC 12 km Community Modeling and Analysis System (CMAQ, Byun and Schere, 2006; Pan et al., 2014) were used to derive isoprene emissions. The NAQFC CMAQ is driven by the NAM meteorological fields, and biogenic emissions are computed online from the Biogenic Emission Inventory System (BEIS) version 3.14, that often produces much lower emissions than MEGAN at the "isoprene volcano" and in eastern Texas (e.g., Warneke et al., 2010; Carlton and Baker, 2011). The NAQFC CMAQ OH performance near the "isoprene volcano" was generally satisfactory for the studied period: i.e., the mean±standard deviation of the predicted OH of $(1.8\pm0.8)\times10^6$ molecule/cm^3 on 11 September and $(1.5\pm0.3)\times10^6$ molecule/cm^3 on 06 September along the Missouri flight paths (to be shown in Sections 3.1 and 3.3) are close in magnitude to the observationally constrained OH concentrations in that area during SEAC[4]RS (e.g., $(1.3\pm0.3)\times10^6$ molecule/cm^3 by Wolfe et al., 2015). Close to the estimated OH concentrations of approximately $2-6\times10^6$ molecule/cm^3 near Houston on 16 September, 2006 (Warneke et al., 2010), the simulated PBL OH on 11 September, 2013 ranged from $\sim1.8\times10^6$ to $\sim4.0\times10^6$ molecule/cm^3 along the P-3B flight tracks around Conroe. The OH levels are higher in late morning and around noon ($>3.1\times10^6$ molecule/cm^3) than in the afternoon ($\sim1.8\times10^6$ molecule/cm^3), qualitatively consistent with the observations in downtown Houston in May 2009 (Czader et al., 2013). The averaged OH for all P-3B flight days is within the range of 11 September, following similar diurnal variability. Little prior knowledge exists on CMAQ OH performance in the Greater Houston area, except the moderate negative biases (with observed-to-modeled ratios of 1.15-1.36) reported by Czader et al. (2013) for May 2009. As their modeling system was configured differently from the NAQFC, the biases of the modeled OH fields from the NAQFC CMAQ system need to be investigated further in the future.

2.3 Evaluation datasets

2.3.1 Ground and aircraft measurements of air temperature, solar radiation, and PBLH

We focus on evaluating the sensitivities of NUWRF air temperature, solar radiation, and PBLH to initialization methods, as they are the most important weather variables to the estimated isoprene emissions. The NUWRF modeled (near-) surface air temperature fields were compared with the National Centers for Environmental Prediction (NCEP) Global Surface Observational Weather Data (also used in Huang et al., 2016), the DC-8 aircraft air temperature measurements, and the 5-minute TCEQ special observations at the Conroe site taken in support of the airborne campaigns. The NUWRF modeled solar radiation was briefly compared with the measurements by pyranometers on board the DC-8 and at Conroe. The NUWRF-simulated PBLH was also roughly compared with the estimated PBLH by: a) the 10-second Differential Absorption Lidar (DIAL)-High Spectral Resolution Lidar (HSRL) measurements on board the DC-8 aircraft during the SEAC[4]RS campaign (Figure 2a), released on 22 October, 2014; and b) the vertical gradients of the in-situ isoprene observations measured on board the P-3B aircraft during DISCOVER-AQ at around the Conroe site at different times of the day (Figure 2d).

2.3.2 Satellite soil moisture and heat flux products

The European Space Agency (ESA) soil moisture Climate Change Initiative (CCI, http://www.esa-soilmoisture-cci.org) project produces daily surface soil moisture data at 0.25°×0.25° horizontal resolution, based on multiple passive and active sensors, as well as by merging both passive and active products. Fang et al. (2016) reported that the merged CCI product exhibited higher anomaly correlation (than the individual active/passive CCI products) with both Noah LSM simulations and in-situ measurements during 2000-2013. Version 02.2 of this merged product, which was released in 2015 and covers the period of 1978-2014, has enhanced spatial and temporal coverage and intercalibration between different instruments. We used this version to evaluate the modeled soil moisture fields and the normalized soil moisture anomalies (as defined in Equation (3)), over the regions where the CCI data quality flag equals zero:

$$\text{Normalized soil moisture (SM) anomaly} = \frac{daily\ SM - monthly\ mean\ SM}{monthly\ SM\ standard\ deviation} \tag{3}$$

Soil moisture controls the partitioning of energy into latent (the energy related to changes in phase) and sensible heat (the energy related to temperature changes) fluxes. To evaluate the appropriateness of NUWRF land initialization, we compared NUWRF modeled absolute heat fluxes and their partitioning (i.e., evaporative ratio, defined as latent heat/(latent heat+sensible heat)) with the Atmosphere-Land Exchange Inversion (ALEXI, Anderson et al., 2007; Hain et al., 2011) retrievals. The ALEXI heat flux product using the NOAA Geostationary Operational Environmental Satellite (GOES) thermal-infrared (TIR) land surface temperature, along with its soil moisture proxy retrievals, is a part of the NOAA operational GOES Evapotranspiration and Drought Product System (http://www.ospo.noaa.gov/Products/land/getd). Although limited to clear-sky conditions, ALEXI provides retrievals over a wide range of vegetation cover on horizontal resolution close to that of NUWRF (i.e., 0.08°×0.08° for this study).

3 Results and discussion

3.1 Case study of 11 September, 2013

We first show a case study on 11 September, 2013, when aircraft measurements were available from both the SEAC[4]RS and DISCOVER-AQ campaigns. For SEAC[4]RS, the DC-8 aircraft sampled over broad areas in the central/southeastern US on this day (Figure 2a), passing the "isoprene volcano" region in Missouri at the early afternoon time (18:30-19:30 UTC/12:30-13:30 local standard time), where mixed layer heights indicated by the DIAL-HSRL instrument were mostly below 2 km. Elevated isoprene concentrations (up to ~10.4 ppbv) were observed by the PTR-MS near the surface (<1 km, a.g.l.). Biomass burning plumes had little interference to these isoprene measurements, as determined by the low acetonitrile concentrations (Figure 2b) in the sampled airmasses. For DISCOVER-AQ, the P-3B repeatedly took measurements at different times of the day around the Conroe site in Houston, an area with slightly denser vegetation than downtown Houston (i.e., ~1m^2/m^2 larger LAI, Figure 2c). The observed isoprene vertical profiles at Conroe indicate the growth of PBLH from the morning (a few hundred meters, a.g.l.) to the afternoon (~2 km, a.g.l.), and ~50% higher near-surface isoprene concentrations in the afternoon (~2.5 ppbv) than in the morning (~1.7 ppbv) (Figure 2d). The CO concentrations in the sampled airmasses were below 200 ppbv (Figure 2e), indicating negligible biomass burning source impacts. Anthropogenic emission sources are mainly located at downtown Houston, where the daytime P-3B aircraft isoprene concentrations (i.e., at the Moody Tower, Deer Park, Channelview spirals) did not exceed ~0.6 ppbv and the isoprene-CO enhancement ratio differed from that in Conroe (Figure 2e). The magnitudes of the downtown aircraft isoprene measurements were slightly lower than most of the nearby surface measurements during the daytime (Figure 2f; locations of these surface sites are shown as triangles in Figure 2c). Measured surface isoprene levels during the daytime were ~twice as high as during the nighttime (~0.2-0.3 ppbv) when biogenic isoprene emissions are at their daily minima. Therefore, we expect that non-biogenic emissions contributed to no more than 0.3 ppbv of the P-3B observed isoprene over that region.

3.1.1 Evaluation of NUWRF surface air temperature, PBLH, soil moisture, and heat fluxes

Figure 3a compares the NUWRF modeled surface air temperature in the central/eastern US with ground observations in the early afternoon where the DC-8 flew past Missouri. The 12 km usual run shows 2-4 °C positive biases in Missouri, which are of the similar magnitudes to the findings by Carlton and Baker (2011) for these regions. These positive biases were dramatically reduced in NUWRF ctrl runs. Evaluation of the modeled air temperature and PBLH along the DC-8 flight paths in Missouri was also performed. Over most aircraft sampling areas, air temperatures from the 12 km usual run are associated with larger positive biases than results from the ctrl runs (Figure S3), corresponding to ~1.5 °C higher Root Mean Square Errors (RMSEs, Table 2). The PBLHs from the ctrl runs are thinner (~0.6 km on average) and less spatially variable. They may be closer to the reality referring to the DIAL-HSRL data in Figure 2a, which can also be uncertain. The higher

resolution 4 km ctrl run generated slightly (~0.04 °C) better air temperature and ~0.02 km thinner mean PBLH than the 12 km ctrl run.

Figure 4a compares the NUWRF modeled daytime surface air temperature at the Conroe site against the TCEQ special measurements, and Table 3 summarizes the statistical evaluation of NUWRF PBLH and surface air temperature
5   performance in Conroe. Similar to the conditions in Missouri, temperatures from the 12 km usual run are positively biased by 1.8-3.0°C during the daytime, and the ctrl runs significantly better captured the observed magnitudes (i.e., with 1.6-1.8 °C lower RMSEs than the 12 km usual run), corresponding to at least ~300 m lower PBLH, which are likely more realistic referring to the observed isoprene vertical profiles. The 4 km ctrl simulation produced noticeably lower air temperature and PBLH at the morning (by up to ~0.5 °C/~170 m) and afternoon (by up to ~2.6 °C/~290 m) times than the 12 km ctrl run.

10   Figure 3b-c compare the CCI daily surface soil moisture fields with the NARR and LIS modeled at the NUWRF initialization time on this day. The NARR soil moisture fields are at least 0.1 m^3/m^3 drier than the LIS-NUWRF systems at the beginning of the simulation (Figure 3b), causing the spurious NUWRF temperature/PBLH fields as described earlier. The impact of initial soil moisture states on simulated temperature at later times is similar to the results in Collow et al. (2014) for the Great Plains in May 2010. Figure 3c shows that the normalized soil moisture anomalies from NARR and LIS
15   overall demonstrate similar spatial patterns, which was difficult to be validated with the CCI product due to small sizes of usable data in September 2013 (Figure S2). This suggests that when downscaling land fields to a different modeling system, adjusting the large-scale dataset based on the climatology (preferably for a much longer record) of both systems would be helpful. This adjustment, sometimes also called "bias-correction", is indeed useful in satellite land data assimilation (e.g., scaling satellite soil moisture before assimilation, based on the climatology of the model and the satellite). Figure 5
20   compares the modeled heat fluxes with ALEXI retrievals, indicating that the usual land initialization method resulted in significantly underpredicted latent heat and overpredicted sensible heat, and the partitioning between these heat fluxes were poorly represented. These evaluation results confirm that the usual land initialization method is inappropriate for this case.

It's worth pointing out that by replacing the WRF-default monthly-mean climatological GVF input with the daily near real-time GVF in the 12 km usual run, we did not find significant changes in the modeled temperature (i.e., <±0.5°C, as shown in
25   Figure S4, right) and PBLH (not shown in figures) fields near the Missouri Ozarks and Conroe, where the GVF differences are within ±0.1 (Figure S4, left). Therefore, soil states at the initialization were the major causes to the different temperature and PBLH fields from the usual and ctrl runs over these regions. In contrast, weather fields over some other central/southeastern US regions, particularly in the eastern Arkansas, are shown very sensitive to this GVF update, with negative (positive) GVF differences resulting in positive (negative) temperature differences. Over these regions, the different
30   weather fields in usual and ctrl runs indicate the net effect of GVF and soil initialization.

11

Figure 4b evaluates the impact of simulation length on the modeled surface air temperature at Conroe, and in this case higher temperature biases were shown in the longer simulation (day 2-forecast) regardless of the land initialization method, especially during the morning and early afternoon times. The RMSEs of daytime air temperatures from the day 2-forecasts are ~0.3 °C higher than the day 1-forecasts. Figure 4c shows the impact of atmospheric IC/LBC on the modeled air temperature. In both 12 km and 4 km grids, replacing the NARR IC/LBC with NAM's resulted in larger temperature amplitude, associated with greater negative biases in the morning and positive biases at around the mid-afternoon. The RMSEs of daytime air temperatures from the NAM-related cases are ~0.2 °C higher than the NARR-related cases. Figures 4a and 4c together also suggest that an inappropriate land initialization for a regional simulation can result in almost ten times larger model errors than using an alternative atmospheric IC/LBC.

The NUWRF modeled solar radiation fields were briefly evaluated. It was found that regional NUWRF solar radiation fields in Missouri from these various runs are vastly similar in the early afternoon local time, and they are >30% (a couple of hundred of W/m^2) larger than the DC-8 measurements. These biases are close to what has been reported by Carlton and Baker (2011), and the WRF-satellite differences in Guenther et al. (2012). The daytime NUWRF solar radiations at Conroe had time-varying biases but on average are a few percent different from the observations, and the photosynthetically active radiation at Conroe differed by up to ~12W/m^2 among these simulations.

3.1.2 NUWRF-MEGAN and observation-derived isoprene emissions in Missouri and Houston

Figure 6a shows the spatial distributions of the MEGAN isoprene emissions driven by these multiple NUWRF simulations, compared with the observation-derived emissions at the early afternoon time, when the DC-8 aircraft sampled at the "isoprene volcano" and isoprene emissions approached their daily maxima. Similar spatial patterns of the MEGAN emissions were produced when different NUWRF runs were used. The emissions based on the 12 km NUWRF usual run are at least 20% larger than those driven by NUWRF ctrl runs, corresponding to a ~2 °C larger positive bias in NUWRF temperature. Such emission sensitivities to the air temperature are close to the magnitudes reported in literature for other regions (Guenther et al., 2006, 2012; Wang et al., 2011). NUWRF-MEGAN emissions are 22-49% higher than the observation-derived emissions along the DC-8 flight tracks, with the 4 km NUWRF ctrl run-based MEGAN emissions the closest to the observation-derived.

Figure 6b shows the spatial distributions of the MEGAN isoprene emissions driven by these different NUWRF runs over Houston near the local standard noon time, the second time P-3B sampled over Conroe on that day, when isoprene emissions almost reached their daily maxima. Similar to the Missouri conditions, the MEGAN emissions driven by the 12 km NUWRF usual run are >20% larger than the cases driven by NUWRF ctrl runs. Figure 7a compares NUWRF-MEGAN daytime isoprene emissions at Conroe. The 12 km NUWRF usual run-based daily peak emissions during local noon/early afternoon times are ~20% higher than the 12 km NUWRF ctrl run-based, the latter of which is closer to the observation-derived. The

12

daytime-integrated emissions derived using the 12 km NUWRF usual run are ~21% higher than the 12 km NUWRF ctrl run-based. Again this discrepancy corresponds to a ~2 °C temperature differences on this day (Figure 4a; Table 3). The emissions driven by the 4 km NUWRF ctrl run are the lowest, with the daytime-integrated and the peak emissions ~40% lower than the 12 km NUWRF ctrl run-based, and they substantially deviate from the observation-derived. This is in part

5 due to the coolest temperature from this NUWRF run, especially in the afternoon, as well as its weaker photosynthetically active radiation than the 12 km simulated (i.e., by ~10 W/m^2 on average during the daytime). This may also be resulting from some limitations of MEGAN's parameterization and uncertainty in its other inputs (e.g., PFT and LAI) on small scale. As illustrated in Figure S5, representation error (i.e., due to different data resolutions) along with neglecting horizontal transport in deriving emissions from aircraft data, also contributed to the discrepancies among the 12 km and 4 km

10 NUWRF- and aircraft-derived emissions.

The impacts of simulation length and atmospheric initialization on NUWRF-MEGAN isoprene emissions at Conroe are generally much smaller than the impact of land initialization (Figures 7b-c), mainly due to the smaller temperature sensitivities (Figures 4b-c): The day-2 forecast derived emissions are higher than the day 1 forecast-based emissions by ~10% in Conroe at the local standard noontime, but their daytime-integrated isoprene emissions differ much less (~1.5%).

15 Daytime maximum emissions disagree by only <±2% in both 12 km and 4 km grids. Noontime isoprene emissions related to NAM and NARR IC/LBC differ by less than 2% in both resolutions, and the daytime-integrated emissions related to NAM IC/LBC are higher than the NARR related by ~0.8% and ~5.2% in 12 km and 4 km grids, respectively.

3.2 Conditions on extended time periods

3.2.1 Conditions on multiple flight days during DISCOVER-AQ in September 2013

20 As the 12 km NUWRF ctrl run-based MEGAN isoprene emissions showed the best agreement with the observation-derived emissions at Conroe on 11 September (Section 3.1), we calculated MEGAN isoprene emissions using this set of NUWRF simulation also for the other eight DISCOVER-AQ flight days when variable meteorological conditions were present (details are in the flight reports at: https://discover-aq.larc.nasa.gov/planning-reports_TX2013.php), and the multi-flight day averaged MEGAN calculations were compared with the P-3B aircraft observation-derived at the Conroe site (Figure 8). The

25 multi-day averaged MEGAN and observation-based emissions are higher than the estimates for 11 September, except in the morning. The multi-day mean morning emissions from MEGAN are ~44% higher than the observation-derived, a larger discrepancy than on 11 September. A possible reason for this morning-time overestimation is that MEGAN does not account for the circadian control that can lower the isoprene emissions from some canopies (Hewitt et al., 2011). At local noontime and afternoon times, unlike the 11 September condition, the multi-day averaged MEGAN emissions were slightly (by <5%)

30 lower than the observation-derived.

3.2.2 September 2013 comparing with decadal mean conditions

We extend the analyses to the interannual variability of drought and vegetation conditions in relation to the isoprene emissions in Conroe. The monthly anomalies were calculated for HCHO column (which is often used to derive biogenic emissions) from the Ozone Monitoring Instrument (OMI, De Smedt et al., 2015), Terra-MODIS LAI, ESA CCI microwave soil moisture and ALEXI TIR soil moisture proxy in September 2013, related to the decadal (2005-2014) September means. Eastern Texas was under extreme drought conditions in September 2011 as indicated by the Palmer Drought Severity Index (http://www.ncdc.noaa.gov/temp-and-precip/drought/historical-palmers.php), which was excluded from the decadal mean calculations as severe drought can reduce or terminate isoprene emissions (Pegoraro et al., 2004) and complicate the anomalies. At Conroe, close-to-1 anomalies are found in September 2013 for the ALEXI and CCI data (~0.99 and ~0.98), and vegetation was slightly thinner than the decadal mean conditions (the LAI anomaly of ~0.96). A much lower than average HCHO column (the anomaly of ~0.77) was observed by OMI in this month. A higher OMI anomaly (~0.99) was found in September 2006 studied by Warneke et al. (2010), under drier conditions (ALEXI and CCI anomalies of ~0.77 and ~0.91, respectively) with denser-than-average vegetation (the LAI anomaly of ~1.07). Note that these interannual differences can be complicated by the uncertainty in these satellite data, and also reflect the possible influences by the temporal changes in non-biogenic VOC emissions, local/regional chemistry, and plant types in this area.

3.3 Uncertainty discussions

In addition to the biases in NUWRF surface air temperature, a number of other factors can affect NUWRF-MEGAN isoprene emission calculations. These include:

a) The outdated PFT data that represent year 2008 conditions and the uncertainty in the MODIS LAI input. Future studies should consider implementing in both (NU)WRF and MEGAN the up-to-date land cover input data, e.g., a recently developed product from the Visible Infrared Imaging Radiometer Suite (Zhang, R., et al., 2016), which is compared with the MODIS input in Figure S1 (lower). It would be also worth performing sensitivity calculations using LAI from (NU)WRF, which is either prescribed to its GVF input or computed by some LSMs.

b) The known positive biases in NUWRF solar radiation fields partially due to the lack of aerosol impacts and the misplaced/missing clouds. It has been shown that implementing certain satellite solar radiation products can reduce the biases in MEGAN emissions for other time periods (Carlton and Baker, 2011; Guenther et al., 2012). Identifying suitable satellite radiation products for this case will be included in future work.

c) As described in Section 2.1, due to the omission of deposition, MEGAN version 2.1 net primary emissions are higher than the net emission flux by a few percent on average, and this bias may be larger at a specific location. Adding that contribution in future emission calculations is important.

d) Other limitations in MEGAN's parameterization which good input data can help better diagnose.

The uncertainties of aircraft observation-derived isoprene emissions are expected to come from:

a) The PTR-MS and PTR-ToF-MS measurements have accuracies of ±5% and ±10%, respectively, which can be propagated to the emission calculations. These were smaller than the ±15% from the Warneke et al. (2010) study.

5 b) The biases introduced from the NAQFC CMAQ OH fields as mentioned in Section 2.2.2, which will need to be investigated further on grid-scale (e.g., by comparing them with other modeling products covering our studied period).

c) As discussed in Warneke et al. (2010), the mixed-PBL approach neglects horizontal transport, which may attribute transported isoprene to the incorrect grid boxes. For this study, observed wind speed along the SEAC[4]RS DC-8 flight path ranged from 0.27 to 5.47 m/s, with the mean value of ~1.68 m/s. The TCEQ 5-minute surface wind speed

10 observations were no larger than <3.5 m/s on 11 September. Assuming isoprene lifetime in this study is ~an hour, the aircraft observed isoprene may be actually emitted from the nearby 1-2 model grids on the 12 km scale. Therefore, this approach introduces an error which may not significantly affect the magnitude of regional emission calculations in Missouri but may have a larger impact on the Conroe case especially on a single day (See the illustration in Figure S4). Developing and applying top-down methods that also account for atmospheric transport should be strongly encouraged.

15 d) As discussed in Warneke et al. (2010), the constant 30% entrainment flux may not be realistic for the regions/times we studied, which needs further validation.

e) Regional non-biogenic emission sources may contribute to 10-20% of the aircraft observed isoprene at Conroe, as estimated by the ground in-situ data (Sections 2.2.1 and 3.1).

f) The mixed-PBL approach assumes complete vertical mixing which may not be true in practice. Additionally, the control

20 run based NUWRF modeled PBLHs (Tables 2-3) were used, possibly associated with uncertainty on a magnitude of a few hundred meters (~20%).

Warneke et al. (2010) estimated the uncertainty of their aircraft observation-derived emissions over Texas to be a factor of 2 (-50%, +100%). We anticipate the uncertainty of ours to be of similar magnitude for the single-day Conroe case, but smaller

25 in the multi-day averaged emissions in Conroe. The regional-averaged aircraft observation-derived emissions over the "isoprene volcano" region (Figure 6a for 11 September, and Figure S6 for 06 September with more descriptions in the figure caption) from this study are close to the result in Wolfe et al. (2015) of 587±73 M C/km^2/h, derived using a different method for similar regions during SEAC[4]RS.

4 Conclusions and suggestions on future direction

30 We performed case studies during the SEAC[4]RS and DISCOVER-AQ Houston field campaigns, showing that a usual method to initialize the Noah LSM (i.e., directly downscaling the land fields from the coarser resolution NARR) led to significant positive biases in the coupled NUWRF (near-) surface air temperature and PBLH around the Missouri Ozarks

15

and Houston, Texas, as well as poorly partitioned latent and sensible heat fluxes. Replacing the land initial conditions with the output from a long-term offline LIS (a flexible land surface modeling and data assimilation framework) simulation effectively reduced the positive biases in NUWRF surface air temperature fields. We also showed that using proper land initialization modified NUWRF surface air temperature errors almost ten times as effectively as applying a different

5   atmospheric initialization method. The LIS-NUWRF based MEGAN version 2.1 isoprene emission calculations were at least 20% lower than those computed from the NARR-initialized NUWRF run, closer to the aircraft observation-derived emissions. Higher resolution MEGAN calculations were prone to amplified discrepancies with the aircraft observation-derived emissions on small scales. This was possibly resulting from some limitations of its parameterization, uncertainty in its inputs on small scale, as well as the representation error and neglecting horizontal transport in deriving emissions from

10 aircraft data.

This study emphasizes the importance of proper land initialization to the coupled atmospheric weather modeling and the follow-on biogenic emission modeling. We anticipate that improved weather fields using the better land initialization approach will also benefit the representation of the other processes (other weather-dependent emission calculations,

15 transport, transformation, deposition) included in air quality modeling, and therefore can help reduce uncertainty in the simulated chemical fields. The study is limited to selected locations and times considering the availability of aircraft data, and the observation-derived emissions may also be associated with large uncertainty. In future, developing methods to combine satellite land and atmospheric chemical data assimilation should be encouraged to further improve air quality modeling and top-down emission estimation over broader regions/extended time periods to help interpret the trends and

20 variability of atmospheric composition. Improved chemistry output from regional models can also help evaluate the current "a priori" used in satellite retrievals, and may serve as an alternative.

It should be noted that many published model comparison studies cited in Section 1 did not adequately assess the impacts of model inputs versus their parameterization. Having more confidence in the weather inputs is beneficial for quantifying the

25 other sources of uncertainties (e.g., parameterization, other input data) of the models that they drive. In future, the impact of atmospheric weather input on emissions computed using other biogenic emission models (e.g., BEIS, future versions of MEGAN) will be explored. Efforts will be made to improve the other inputs data (e.g., radiation, land cover).

Although we recommend initializing WRF or NUWRF with the LIS land fields, when long-term atmospheric forcing data

30 are not available to facilitate the offline LIS spin-up, we suggest: 1) "bias-correcting" the land fields from the initial condition model, based on the climatology of the initial condition model and the target model; or 2) adopting the self spin-up method, i.e., running the model for a certain spinup period (e.g., a month) at least once, cycling its own soil variables, to allow the land variables to develop appropriate spatial variability (Angevine et al., 2014). Experiments using simulations with different LSMs along with suitable nudging methods can also be helpful.

5 Model and data availability

Instructions for obtaining and running the used models can be found at: LIS (lis.gsfc.nasa.gov/documentation/lis); NUWRF (nuwrf.gsfc.nasa.gov/doc); MEGAN (lar.wsu.edu/megan/docs). The satellite land products, and the NUWRF/MEGAN output can be made available upon request. The open access to the used aircraft and ground observations is acknowledged:

5 Aircraft data were obtained from: http://www-air.larc.nasa.gov/index.html

SEAC[4]RS: doi: 10.5067/Aircraft/SEAC4RS/Aerosol-TraceGas-Cloud

DISCOVER-AQ: doi: 10.5067/Aircraft/DISCOVER-AQ/Aerosol-TraceGas

TCEQ AutoGC data: https://www.tceq.texas.gov/cgi-bin/compliance/monops/agc_daily_summary.pl

NCEP Global Surface Observational Weather Data (DS461): http://rda.ucar.edu/datasets/ds461.0/

10 OMI HCHO column data: http://h2co.aeronomie.be

Appendix: List of acronyms by category

A.1 Model related (with short descriptions in the parentheses)

Models

BEIS (emission model): Biogenic Emission Inventory System

15 LIS (land surface modeling and data assimilation framework): Land Information System

MEGAN (emission model): Model of Emissions of Gases and Aerosols from Nature

Noah LSM (land surface model): NCAR, OSU, AirForce, office of Hydrology Land Surface Model

NAQFC CMAQ (regional air quality model): National Air Quality Forecasting Capability Community Modeling and Analysis System

20 NUWRF (observation-driven regional earth system modeling and assimilation system): NASA-Unified Weather Research and Forecasting model

Model forcing datasets

GDAS (LIS forcing): Global Data Assimilation System

GLDAS (LIS forcing): Global Land Data Assimilation System

25 IC/LBC: Initial Conditions/Lateral Boundary Conditions

NAM (NUWRF forcing): North American Mesoscale Forecast System

NARR (NUWRF forcing): North American Regional Reanalysis

A.2 Observation related (measurements used in this study are indicated in the parentheses)

30 *Field experiments and aircraft instruments*

DC-8 and P-3B: Aircraft used in SEAC[4]RS and DISCOVER-AQ, respectively

DIAL-HSRL (PBLH): Differential Absorption Lidar-High Spectral Resolution Lidar

DISCOVER-AQ: Deriving Information on Surface Conditions from COlumn and VERtically Resolved Observations Relevant to Air Quality

SEAC[4]RS: Studies of Emissions and Atmospheric Composition, Clouds and Climate Coupling by Regional Surveys

5   PTR-MS (isoprene): Proton Transfer Reaction-Mass Spectrometry

PTR-ToF-MS (isoprene): Proton-Transfer-Reaction Time-of-Flight Mass Spectrometry

Satellite related

ALEXI (heat flux, soil moisture proxy): Atmosphere-Land Exchange Inversion

CCI (soil moisture): Climate Change Initiative

10   GOES: Geostationary Operational Environmental Satellite

MODIS (land use/land cover, LAI, GVF): Moderate Resolution Imaging Spectroradiometer

OMI (HCHO): Ozone Monitoring Instrument

TIR: Thermal Infrared

VIIRS (land use/land cover): Visible Infrared Imaging Radiometer Suite

15   *Surface Measurements*

AutoGC (isoprene): Automated Gas Chromatograph

A.3 Terminology

BVOCs: biogenic volatile organic compounds

20   CH_4: methane

CO: carbon monoxide

CO_2: carbon dioxide

GVF: green vegetation fraction

HCHO: formaldehyde

25   LAI: leaf area index

NDVI: normalized difference vegetation index

N_2O: nitrous oxide

OH: hydroxyl radical

O_3: ozone

30   PBLH: planetary boundary layer height

PFT: plant functional type

RMSE: root mean square error

SM: soil moisture

232-MBO: 2,3,2-methylbutenol

A.4 Organizations/Agencies/Geographical regions

CONUS: contiguous United States

ESA: European Space Agency

5 NA: North America

NASA: National Aeronautics and Space Administration

NCEP: National Centers for Environmental Prediction

NOAA: National Oceanic and Atmospheric Administration

TCEQ: Texas Commission on Environmental Quality

10 TX: State of Texas

References

Anderson, M.C., J.M. Norman, J.R. Mecikalski, J.P. Otkin, and W.P. Kustas (2007), A climatological study of surface fluxes and moisture stress across the continental United States based on thermal infrared remote sensing, Part I: model formulation, J. Geophys. Res., 112, D11112.

25

Angevine, W. M., Eddington, L., Durkee, K., Fairall, C., Bianco, L., and Brioude, J. (2012), Meteorological model evaulation for CalNex 2010, Mon. Weather Rev., 140, 3885–3906, doi:10.1175/MWRD-12-00042.1.

Angevine, W. M., Bazile, E., Legain, D., and Pino, D. (2014), Land surface spinup for episodic modeling, Atmos. Chem. 30 Phys., 14, 8165-8172, doi:10.5194/acp-14-8165-2014.

Bell, J. R., Case, J. L., LaFontaine, F. J., Kumar, S. V. (2012), Evaluating the Impacts of NASA/SPoRT Daily Greenness Vegetation Fraction on Land Surface Model and Numerical Weather Forecasts, the 16th Symposium on Integrated Observing and Assimilation Systems for Atmosphere, Oceans, and Land Surface, New Orleans, LA, 22−26 January 2012, http://ntrs.nasa.gov/archive/nasa/casi.ntrs.nasa.gov/20120004024.pdf (last access: January 2017).

Byun, D. and Schere, K. L. (2006), Review of the Governing Equations, Computational Algorithms, and Other Components of the Models-3 Community Multiscale Air Quality (CMAQ) Modeling System, Appl. Mech. Rev., 59, 51–77, doi: doi:10.1115/1.2128636.

Byun, D., Kim, H.-C., Ngan, F. (2011), Final Report: Improvement of Meteorological Modeling by Accurate Prediction of Soil Moisture in the Weather Research and Forecasting (WRF) Model, available at: https://www.tceq.texas.gov/assets/public/implementation/air/am/contracts/reports/mm/582886246FY1009-NOAA_WRF_Soil_Moisture_20110331.pdf, reported by NOAA ARL to Texas Commission on Environmental Quality (last access: January 2017).

Canty, T. P., Hembeck, L., Vinciguerra, T. P., Anderson, D. C., Goldberg, D. L., Carpenter, S. F., Allen, D. J., Loughner, C. P., Salawitch, R. J., and Dickerson, R. R. (2015), Ozone and NO_x chemistry in the eastern US: evaluation of CMAQ/CB05 with satellite (OMI) data, Atmos. Chem. Phys., 15, 10965-10982, doi:10.5194/acp-15-10965-2015.

Carlton, A. G. and K. R. Baker (2011), Photochemical Modeling of the Ozark Isoprene Volcano: MEGAN, BEIS, and Their Impacts on Air Quality Predictions, Environ. Sci. Technol., 45 (10), 4438-4445, doi: 10.1021/es200050x.

Case, J., W. Crosson, S. V. Kumar, W. Lapenta, and C. Peters-Lidard (2008), Impacts of High-Resolution Land Surface Initialization on Regional Sensible Weather Forecasts from the WRF Model, J. Hydrometeorology, 9 (6), 1249-1266, doi: 10.1175/2008JHM990.1.

Case, J. L., S. V. Kumar, J. Srikishen, and G. J. Jedlovec (2011), Improving numerical weather predictions of summertime precipitation over the southeastern United States through a high-resolution initialization of the surface state, Weather Forecasting, 26, 785–807, doi:10.1175/ 2011WAF2222455.1.

Chen, F., and J. Dudhia (2001), Coupling an advanced land surface-hydrology model with the Penn State-NCAR MM5 modeling system. Part I: Model implementation and sensitivity, Mon. Wea. Rev., 129, 569-585, doi:10.1175/1520-0493(2001)129<0569:CAALSH>2.0.CO;2.

Collow, T. W., A. Robock, and W. Wu (2014), Influences of soil moisture and vegetation on convective precipitation forecasts over the United States Great Plains, J. Geophys. Res. Atmos., 119, 9338–9358, doi:10.1002/2014JD021454.

5 Crawford, J. H., R. R. Dickerson, and J. C. Hains (2014), DISCOVER-AQ: Observations and early results, Environ. Managers, September 2014, 8-15.

Czader, B. H., X. Li, and B. Rappenglueck (2013), CMAQ modeling and analysis of radicals, radical precursors, and chemical transformations, J. Geophys. Res. Atmos., 118, 11,376–11,387, doi:10.1002/jgrd.50807.

10

De Gouw, J. and Warneke, C. (2007), Measurements of volatile organic compounds in the earth's atmosphere using proton-transferreaction mass spectrometry, Mass Spectrom. Rev., 26, 223–257, doi:10.1002/mas.20119.

De Smedt, I., Stavrakou, T., Hendrick, F., Danckaert, T., Vlemmix, T., Pinardi, G., Theys, N., Lerot, C., Gielen, C.,
15 Vigouroux, C., Hermans, C., Fayt, C., Veefkind, P., Müller, J.-F., and Van Roozendael, M. (2015), Diurnal, seasonal and long-term variations of global formaldehyde columns inferred from combined OMI and GOME-2 observations, Atmos. Chem. Phys., 15, 12519-12545, doi:10.5194/acp-15-12519-2015.

Duncan, B. N., Y. Yoshida, M. R. Damon, A. R. Douglass, and J. C. Witte (2009), Temperature dependence of factors
20 controlling isoprene emissions, Geophys. Res. Lett., 36, L05813, doi:10.1029/2008GL037090.

Ek, M. B., K. E. Mitchell, Y. Lin, E. Rogers, P. Grunmann, V. Koren, G. Gayno, and J. D. Tarpley (2003), Implementation of Noah land surface model advances in the National Centers for Environmental Prediction operational mesoscale Eta model, J. Geophys. Res., 108, 8851, doi:10.1029/2002JD003296, D22.

25

Emmerson, K. M., Galbally, I. E., Guenther, A. B., Paton-Walsh, C., Guerette, E.-A., Cope, M. E., Keywood, M. D., Lawson, S. J., Molloy, S. B., Dunne, E., Thatcher, M., Karl, T., and Maleknia, S. D. (2016), Current estimates of biogenic emissions from eucalypts uncertain for southeast Australia, Atmos. Chem. Phys., 16, 6997-7011, doi:10.5194/acp-16-6997-2016.

30

Fang, L., C. R. Hain, X. Zhan, and M. C. Anderson (2016), An inter-comparison of soil moisture data products from satellite remote sensing and a land surface model, International Journal of Applied Earth Observation and Geoinformation, 48, 37-50, doi: 10.1016/j.jag.2015.10.006.

Fiore, A. M., Levy II, H., and Jaffe, D. A. (2011), North American isoprene influence on intercontinental ozone pollution, Atmos. Chem. Phys., 11, 1697-1710, doi:10.5194/acp-11-1697-2011.

Guenther, A., Karl, T., Harley, P., Wiedinmyer, C., Palmer, P. I., and Geron, C. (2006), Estimates of global terrestrial isoprene emissions using MEGAN (Model of Emissions of Gases and Aerosols from Nature), Atmos. Chem. Phys., 6, 3181-3210, doi:10.5194/acp-6-3181-2006.

Guenther, A. B., X. Jiang, C. L. Heald, T. Sakulyanontvittaya, T. Duhl, L. K. Emmons, and X. Wang (2012), The Model of Emissions of Gases and Aerosols from Nature version 2.1 (MEGAN2.1): an extended and updated framework for modeling biogenic emissions, Geosci. Model Dev., 5 (6), 1471-1492, doi:10.5194/gmd-5-1471-2012.

Hain, C. R., W. T. Crow, J. R. Mecikalski, M. C. Anderson, and T. Holmes (2011), An intercomparison of available soil moisture estimates from thermal infrared and passive microwave remote sensing and land surface modeling, J. Geophys. Res., 116, D15107, doi:10.1029/2011JD015633.

Hain, C. R., W. T. Crow, M. C. Anderson, and J. R. Mecikalski (2012), An ensemble Kalman filter dual assimilation of thermal infrared and microwave satellite observations of soil moisture into the Noah land surface model, Water Resour. Res., 48, W11517, doi:10.1029/2011WR011268.

Hewitt, C.N., K. Ashworth, A. Boynard, A. Guenther, B. Langford, A. R. MacKenzie, P. K. Misztal, E. Nemitz, S. M. Owen, M. Possell, T. A. M. Pugh, A. C. Ryan, and O. Wild (2011), Ground-level ozone influenced by circadian control of isoprene emissions, Nature Geoscience, 4, 671-674, doi:10.1038/ngeo1271.

Hogrefe, C., Isukapalli, S., Tang, X., Georgopoulos, P., He, S., Zalewsky, E., Hao, W., Ku, J., Key, T., and Sistla, G. (2011), Impact of biogenic emission uncertainties on the simulated response of ozone and fine Particulate Matter to anthropogenic emission reductions, J. Air Waste Manage., 61, 92-108, doi: 10.3155/1047-3289.61.1.92.

Huang, M., Carmichael, G. R., Chai, T., Pierce, R. B., Oltmans, S. J., Jaffe, D. A., Bowman, K. W., Kaduwela, A., Cai, C., Spak, S. N., Weinheimer, A. J., Huey, L. G., and Diskin, G. S. (2013), Impacts of transported background pollutants on summertime western US air quality: model evaluation, sensitivity analysis and data assimilation, Atmos. Chem. Phys., 13, 359-391, doi:10.5194/acp-13-359-2013.

22

Huang, M., P. Lee, R. McNider, J. Crawford, E. Buzay, J. Barrick, Y. Liu, and P. Krishnan (2016), Temporal and spatial variability of daytime land surface temperature in Houston: Comparing DISCOVER-AQ aircraft observations with the WRF model and satellites, J. Geophys. Res. Atmos., 121, 185–195, doi:10.1002/2015JD023996.

5   Iacono, M. J., J. S. Delamere, E. J. Mlawer, M. W. Shephard, S. A. Clough, and W. D. Collins (2008), Radiative forcing by long-lived greenhouse gases: Calculations with the AER radiative transfer models, J. Geophys. Res., 113, D13103, doi:10.1029/2008JD009944.

Janjic, Z. I. (2000), Comments on "Development and Evaluation of a Convection Scheme for Use in Climate Models", J.
10   Atmos. Sci., 57, 3686, doi:10.1175/1520-0469(2000)057<3686:CODAEO>2.0.CO;2.

Janjic, Z. I. (2002), Nonsingular Implementation of the Mellor–Yamada Level 2.5 Scheme in the NCEP Meso model, NCEP Office Note, No. 437, 61.

15   Janjic, Z. I. (2003), A nonhydrostatic model based on a new approach, Meteorol. Atmos. Phys., 82, 271–285, doi:10.1007/s00703-001- 0587-6.

Janjic, Z., Black, T., Pyle, M., Chuang, H., Rogers, E., and DiMego, G. (2004), An Evolutionary Approach to Nonhydrostatic Modeling, Symposium on the 50th Aniversary of Operational Numerical Weather Prediction, College Park,
20   MD,   Amer.   Meteor.   Soc,   available   at: http://www.wrf-model.org/wrfadmin/publications/Chuang_Janjic_NWP50yearsfinalshort.pdf (last access: January 2017).

Jin, J., Miller, N. L., and Schlegel, N. (2010), Sensitivity Study of Four Land Surface Schemes in the WRF model, Advances in Meteorology, vol. 2010, Article ID 167436, 11 pages, 2010. doi:10.1155/2010/167436.
25

Karl, T. G., A. Guenther, R. J. Yokelson, J. Greenberg, M. Potosnak, D. R. Blake, and P. Artaxo (2007), The tropical forest and fire emissions experiment: Emission, chemistry, and transport of biogenic volatile organic compounds in the lower atmosphere over Amazonia, J. Geophys. Res., 112, D18302, doi:10.1029/2007JD008539.

30   Kennedy, A. D., Dong, X., Xi, B., Xie, S., Zhang, Y., and Chen, J. (2011), A Comparison of MERRA and NARR Reanalyses   with   the   DOE   ARM   SGP   Data,   Journal   of   Climate,   24,   4541-4557,   doi: http://dx.doi.org/10.1175/2011JCLI3978.1.

Kumar, S. V., Y. Tian, C. Peters-Lidard, et al., (2006), Land information system: An interoperable framework for high resolution land surface modeling, Environ Modelling Software, 21, 1402-1415, doi: 10.1016/j.envsoft.2005.07.004.

Kumar, S. V., C. Peters-Lidard, Y. Tian, et al. (2008), An Integrated Hydrologic Modeling and Data Assimilation Framework, Computer, 41 (12): 52-59, doi: 10.1109/MC.2008.475.

Lee, E., R. Bieda, J. Shanmugasundaram, and H. Basara Richter (2016), Land surface and atmospheric conditions associated with heat waves over the Chickasaw Nation in the South Central United States, J. Geophys. Res. Atmos., 121, 6284–6298, doi:10.1002/2015JD024659.

Li, G., R. Zhang, J. Fan, and X. Tie (2007), Impacts of biogenic emissions on photochemical ozone production in Houston, Texas, J. Geophys. Res., 112, D10309, doi:10.1029/2006JD007924.

Lin, T.-S. and Cheng, F.-Y. (2015), Impact of soil moisture initialization and soil texture on simulated land-atmosphere interaction in Taiwan, Journal of Hydrometeorology, doi: http://dx.doi.org/10.1175/JHM-D-15-0024.1.

McQueen, J., Huang, J., Shafran, P., Rogers, E., Pondeca, M., DiMego, G., and Stajner, I. (2015a), Evaluation of NCEP Atmospheric Models for Driving Air Quality Prediction, 27th Conference on Weather Analysis and Forecasting, Chicago, IL, available at: https://ams.confex.com/ams/27WAF23NWP/webprogram/Paper273598.html (last access: December 2016).

McQueen, J., Lee, P., Huang, J., Huang, H.-C., Shafran, P., Rogers, E., Pondeca, M., DiMego, G., and Stajner, I. (2015b), NWS NWP models and their Potential Impact for Air Quality Prediction, 7th International workshop on air quality research, College Park, MD, available at: http://www.arl.noaa.gov/documents/IWAQFR/Presentations2015/S4_McQueen_IWAQFR_2015.pdf (last access: December 2016).

Mesinger, F., DiMego, G., Kalnay, E., Mitchell, K., Shafran, P. C., Ebisuzaki, W., Jovic, D., Woollen, J., Rogers, E., Berbery, E. H., Ek, M. B., Fan, Y., Grumbine, R., Higgins, W., Li, H., Lin, Y., Manikin, G., Parrish, D., and Shi, W. (2006), North American Regional Reanalysis, B. Am. Meteor. Soc., 87, 343–360, doi:10.1175/BAMS-87-3-343.

Millet, D. B., D. J. Jacob, K. F. Boersma, T. M. Fu, T. P. Kurosu, K. Chance, C. L. Heald, and A. Guenther (2008), Spatial distribution of isoprene emissions from North America derived from formaldehyde column measurements by the OMI satellite sensor, J. Geophys. Res., 113, D02307, doi:10.1029/2007JD008950.

Miralles, D. G., M. J. van den Berg, A. J. Teuling, and R. A. M. de Jeu (2012), Soil moisture-temperature coupling: A multiscale observational analysis, Geophys. Res. Lett., 39, L21707, doi:10.1029/2012GL053703.

Monin, A. S., and A. M. Obukhov (1954), Basic laws of turbulent mixing in the surface layer of the atmosphere, Tr. Akad.
5   Nauk. SSSR Geophiz. Inst., 24 (151), 163–187.

Müller, M., Mikoviny, T., Feil, S., Haidacher, S., Hanel, G., Hartungen, E., Jordan, A., Märk, L., Mutschlechner, P., Schottkowsky, R., Sulzer, P., Crawford, J. H., and Wisthaler, A. (2014), A compact PTR-ToF-MS instrument for airborne measurements of volatile organic compounds at high spatiotemporal resolution, Atmos. Meas. Tech., 7, 3763-3772,
10   doi:10.5194/amt-7-3763-2014.

Palmer, P. I., D. J. Jacob, A. M. Fiore, R. V. Martin, K. Chance, and T. P. Kurosu (2003), Mapping isoprene emissions over North America using formaldehyde column observations from space, J. Geophys. Res., 108(D6), 4180, doi:10.1029/2002JD002153.
15

Pan, L., Tong, D. Q., Lee, P., Kim, H., and Chai, T. (2014), Assessment of NO_x and O_3 forecasting performances in the U.S. National Air Quality Forecasting Capability before and after the 2012 major emissions updates, Atmos. Environ., 95, 610–619, doi: 10.1016/j.atmosenv.2014.06.020.

20   Pegoraro, E., Rey, A., Greenberg, J., Harley, P., Grace, J., Malhi, Y., and Guenther, A. (2004), Effect of drought on isoprene emission rates from leaves of Quercus virginiana Mill, Atmos. Environ., 38, 6149–6156, doi:10.1016/j.atmosenv.2004.07.028.

Peters-Lidard, C.D., E. M. Kemp, T. Matsui, J. A. Santanello, Jr., S. V., Kumar, J. P. Jacob, T. Clune, W.-K. Tao, M. Chin,
25   A. Hou, J. L. Case, D. Kim, K.-M. Kim, W. Lau, Y. Liu, J.-J. Shi, D. Starr, Q. Tan, Z. Tao, B. F. Zaitchik, B. Zavodsky, S. Q. Zhang, and M. Zupanski (2015), Integrated modeling of aerosol, cloud, precipitation and land processes at satellite-resolved scales, Environmental Modelling & Software, 67, 149–159, doi: 10.1016/j.envsoft.2015.01.007.

Rodell, M., Houset, P. R., Berg, A. A., and Famiglietti, J.S. (2005), Evaluation of 10 Methods for Initializing a Land Surface
30   Model, Journal of Hydrometeorology, 6, 146-155, doi: http://dx.doi.org/10.1175/JHM414.1.

Rogers, E., T. Black, B. Ferrier, Y. Lin, D. Parrish, and G. DiMego (2001), Changes to the NCEP Meso Eta analysis and forecast system: Increase in resolution, new cloud microphysics, modified precipitation assimilation, modified 3DVAR analysis, NWS Technical Procedures Bulletin, available at: http://www.emc.ncep.noaa.gov/mmb/mmbpll/eta12tpb (last access: December 2016).

5

Royer, A., and S. Poirier (2010), Surface temperature spatial and temporal variations in North America from homogenized satellite SMMR-SSM/I microwave measurements and reanalysis for 1979–2008, J. Geophys. Res., 115, D08110, doi:10.1029/2009JD012760.

10   Saide, P. E., Carmichael, G. R., Spak, S. N., Gallardo, L., Osses, A. E., Mena-Carrasco, M. A., and Pagowski, M. (2011), Forecasting urban PM10 and PM2.5 pollution episodes in very stable nocturnal conditions and complex terrain using WRFChem CO tracer model, Atmos. Environ., 45, 2769–2780, doi:10.1016/j.atmosenv.2011.02.001.

Santanello, J. A., S. V. Kumar, C. D. Peters-Lidard, K. W. Harrison, and S. Zhou (2013), Impact of Land Model Calibration
15   on Coupled Land–Atmosphere Prediction, J. Hydrometeorology, 14 (5), 1373-1400, doi: 10.1175/JHM-D-12-0127.1.

Santanello, J. A., S. V. Kumar, C. D. Peters-Lidard, and P. M. Lawston (2016), Impact of Soil Moisture Assimilation on Land Surface Model Spinup and Coupled Land-Atmosphere Prediction, J. Hydrometeorology, doi:10.1175/jhm-d-15-0072.1.

20

Skamarock, W., J.B. Klemp, J. Dudhia, D.O. Gill, D. Barker, M.G. Duda, X.-Y. Huang, and W. Wang (2008), A Description of the Advanced Research WRF Version 3, NCAR Technical Note NCAR/TN-475+STR, doi:10.5065/D68S4MVH.

25   Sindelarova, K., Granier, C., Bouarar, I., Guenther, A., Tilmes, S., Stavrakou, T., Müller, J.-F., Kuhn, U., Stefani, P., and Knorr, W. (2014), Global data set of biogenic VOC emissions calculated by the MEGAN model over the last 30 years, Atmos. Chem. Phys., 14, 9317-9341, doi:10.5194/acp-14-9317-2014.

Tao, Z., J. A. Santanello, M. Chin, S. Zhou, Q. Tan, E. M. Kemp, and C. D. Peters-Lidard (2013), Effect of land cover on
30   atmospheric processes and air quality over the continental United States – a NASA Unified WRF (NU-WRF) model study. Atmospheric Chemistry and Physics, 13, 6207-6226, doi:10.5194/acp-13-6207-2013.

Toon, O. B., H. Maring, J. Dibb, R. Ferrare, D. J. Jacob, E. J. Jensen, Z. J. Luo, G. G. Mace, L. L. Pan, L. Pfister, K. H. Rosenlof, J. Redemann, J. S. Reid, H. B. Singh, A. M. Thompson, R. Yokelson, P. Minnis, G. Chen, K. W. Jucks and A.

26

Pszenny (2016), Planning, implementation, and scientific goals of the Studies of Emissions and Atmospheric Composition, Clouds and Climate Coupling by Regional Surveys (SEAC[4]RS) field mission, J. Geophys. Res. Atmos., 121, 4967–5009, doi:10.1002/2015JD024297.

5   Wang, X., Situ, S., Guenther, A. B., Chen, F., Wu, Z., Xia, B., and Wang, T. (2011), Spatiotemporal variability of biogenic terpenoid emissions in Pearl River Delta, China, with high-resolution land-cover and meteorological data, Tellus B, 63, 241–254, doi: 10.1111/j.1600-0889.2010.00523.x.

Warneke, C., J. A. de Gouw, L. Del Negro, J. Brioude, S. McKeen, H. Stark, W. C. Kuster, P. D. Goldan, M. Trainer, F. C. 10 Fehsenfeld, C. Wiedinmyer, A. B. Guenther, A. Hansel, A. Wisthaler, E. Atlas, J. S. Holloway, T. B. Ryerson, J. Peischl, L. G. Huey, and A. T. Case Hanks (2010), Biogenic emission measurement and inventories determination of biogenic emissions in the eastern United States and Texas and comparison with biogenic emission inventories, J. Geophys. Res., 115, D00F18, doi:10.1029/2009JD012445.

15 Wiedinmyer, C., J. Greenberg, A. Guenther, B. Hopkins, K. Baker, C. Geron, P. I. Palmer, B. P. Long, J. R. Turner, G. Pétron1, P. Harley, T. E. Pierce, B. Lamb, H. Westberg, W. Baugh, M. Koerber, and M. Janssen (2005), Ozarks Isoprene Experiment (OZIE): Measurements and modeling of the "isoprene volcano", J. Geophys. Res., 110, D18307, doi:10.1029/2005JD005800.

20 Wolfe, G. M., T. F. Hanisco, H. L. Arkinson, T. P. Bui, J. D. Crounse, J. Dean-Day, A. Goldstein, A. Guenther, S. R. Hall, G. Huey, D. J. Jacob, T. Karl, P. S. Kim, X. Liu, M. R. Marvin, T. Mikoviny, P. K. Misztal, T. B. Nguyen, J. Peischl, I. Pollack, T. Ryerson, J. M. St. Clair, A. Teng, K. R. Travis, K. Ullmann, P. O. Wennberg, and A. Wisthaler (2015), Quantifying sources and sinks of reactive gases in the lower atmosphere using airborne flux observations, Geophys. Res. Lett., 42, 8231–8240, doi:10.1002/2015GL065839.
25

Yu, M., Carmichael, G. R., Zhu, T., Cheng, Y. (2012), Sensitivity of predicted pollutant levels to urbanization in China, Atmos. Environ., 60, 544-554, 1352-2310, doi: 10.1016/j.atmosenv.2012.06.075.

Zaitchik, B. F., J. A. Santanello, S. V. Kumar, and C. D. Peters-Lidard (2012), Representation of Soil Moisture Feedbacks 30 during Drought in NASA Unified WRF (NU-WRF), J. Hydrometeor, 14 (1), 360-367, doi: 10.1175/JHM-D-12-069.1.

Zeng, X.-M., Wang, B., Zhang, Y., Song, S., Huang, X., Zheng, Y., Chen, C., and Wang, G. (2014), Sensitivity of high-temperature weather to initial soil moisture: a case study using the WRF model, Atmos. Chem. Phys., 14, 9623-9639, doi:10.5194/acp-14-9623-2014.

Zhang, R., Huang, C., Zhan, X., Dai, Q., and Song, K. (2016), Development and validation of the global surface type data product from S-NPP VIIRS, Remote Sens. Lett., 7, 51-60, doi: 10.1080/2150704X.2015.1101649.

5   Zhang, Y., Y. Wang, G. Chen, C. Smeltzer, J. Crawford, J. Olson, J. Szykman, A. J. Weinheimer, D. J. Knapp, D. D. Montzka, et al. (2016), Large vertical gradient of reactive nitrogen oxides in the boundary layer: Modeling analysis of DISCOVER-AQ 2011 observations, J. Geophys. Res. Atmos., 121, 1922–1934, doi:10.1002/2015JD024203.

Figures
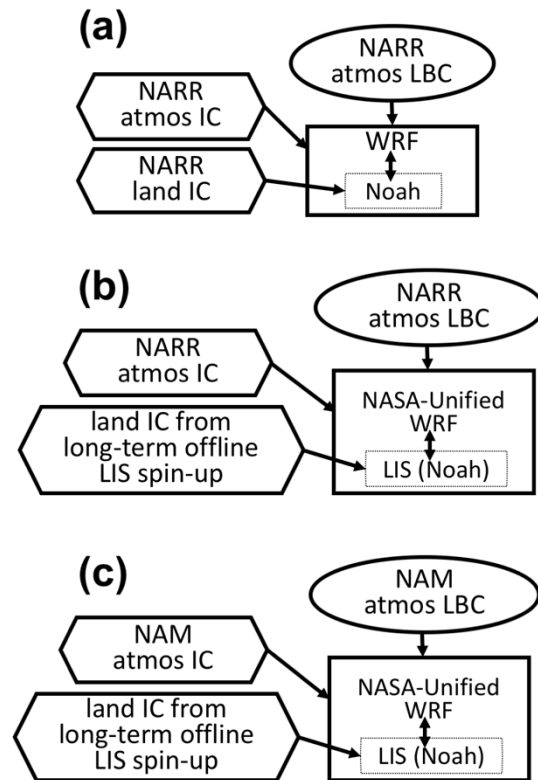
Figure 1: Illustration of the different (NU)WRF initialization methods compared in this study: (a) A usual method, applied only on a 12 km resolution grid, in which the land and atmospheric (atmos) initial conditions (IC) and lateral boundary conditions (LBC) are downscaled from a coarser model output North American Regional Reanalysis (NARR). (b) The ctrl runs on 12 km and 4 km resolution grids, in which the land IC are from long-term offline LIS spin-up at the same grid resolutions as NUWRF, forced by highly resolved atmospheric forcing and precipitation data; atmospheric IC and LBC are from NARR. (c) Same as (b), except that atmospheric IC and LBC are from the North American Mesoscale Forecast System (NAM). Table 1 summarizes all NUWRF simulations in this study including the corresponding initialization methods illustrated here.
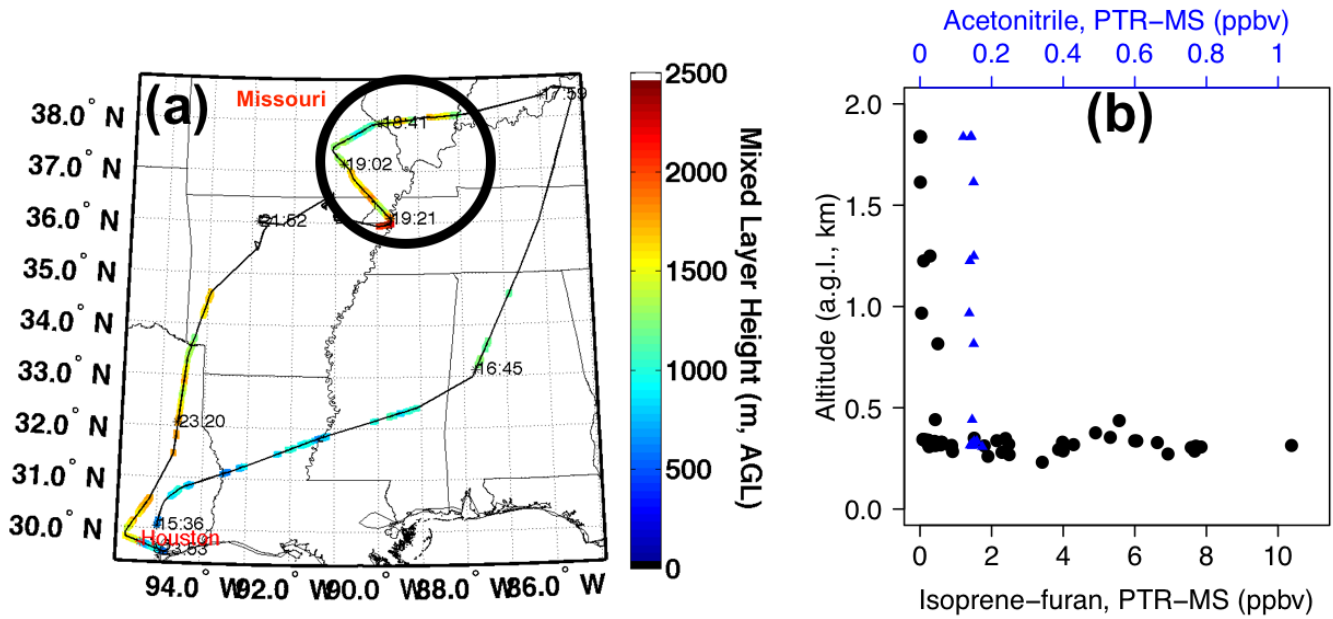
Figure 2: Measurements during the SEAC[4]RS campaign on 11 September, 2013: (a) the DC-8 flight path colored by mixed layer height from the DIAL-HSRL instrument. Areas within the black circle indicate the Missouri "isoprene volcano" regions sampled at ~19 UTC (~13 local standard time). (b) Vertical profiles of the PTR-MS measured isoprene (black dots) and acetonitrile (blue triangles) at around the "isoprene volcano" regions.
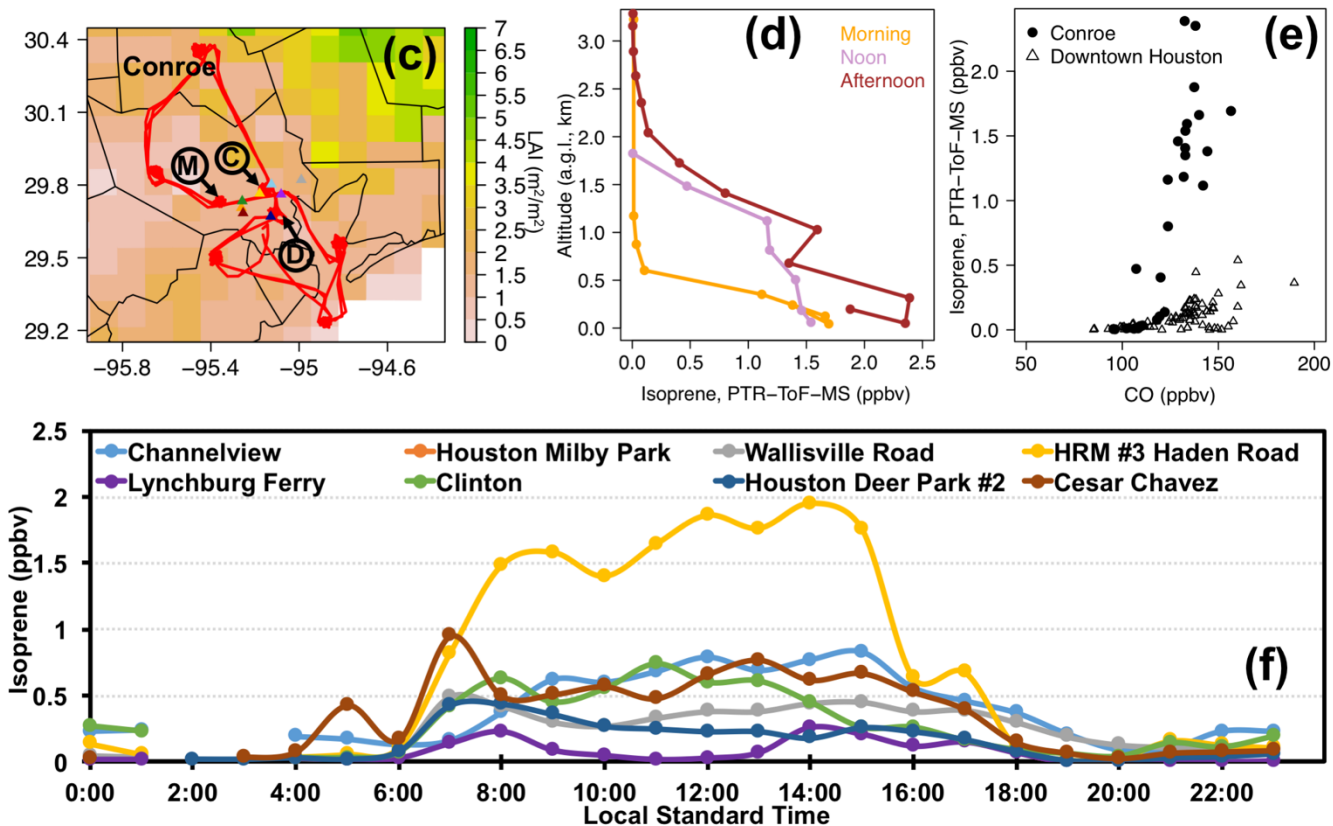
Figure 2 (cont.): Measurements during the DISCOVER-AQ Houston campaign on 11 September, 2013: (c) MODIS leaf area index (8-day mean with missing values filled with the monthly mean) over the Greater Houston area in the 12 km NUWRF grid. The red solid line indicates the DISCOVER-AQ P-3B flight path. (d) Vertical profiles of the PTR–ToF–MS measured isoprene at the Conroe spirals in the Greater Houston area at different times of the day. (e) Scatterplot of the P-3B measured isoprene-CO at the Conroe spirals (filled circles) and at three downtown Houston/Ship Channel sites of Moody Tower, Deer Park and Channelview (open triangles), on 11 September, 2013. Locations of Conroe, Moody Tower (M), Deer Park (D) and Channelview (C) are defined in Figure 2c. The CO measurements were taken using a Diode laser spectrometer measurements of CO, CH_4, N_2O instrument with uncertainty of 2% or 2 ppbv. (f) AutoGC isoprene measurements at multiple surface sites in Houston urban and ship channel areas. Locations of these sites are shown in Figure 2c as colored triangles. Note that only one AutoGC data point is available at the Milby Park site at 00 local standard time.
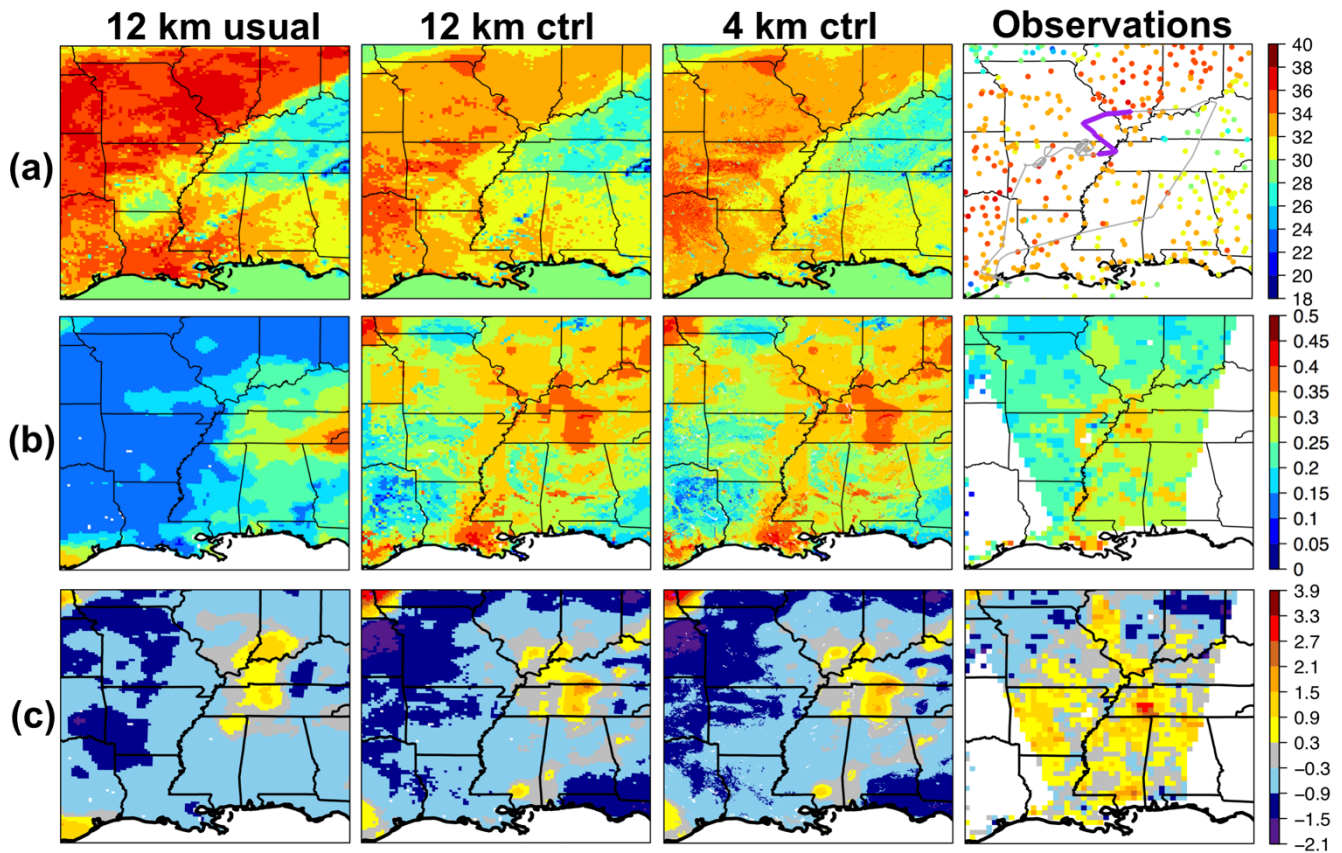
Figure 3: Evaluation of NUWRF (a) surface air temperature in °C at ~13 local standard time (b) surface soil moisture in m^3/m^3 and (c) normalized surface soil moisture at ~00 local standard time (NUWRF initial time) over the central/southeastern US on 11 September, 2013. NUWRF simulations are shown in the first three columns; NCEP surface in-situ temperature observations and the ESA CCI combined daily soil moisture product (0.25°×0.25°, only showing data with quality flag = 0) are shown in the right column. The uncertainty of the CCI product on 11 September, 2013 is shown in Figure S2 (left). The normalized anomaly is defined in Eq. (3) in the text, and Figure S2 (right) shows the size of usable CCI data in September 2013. Note that for (b) and (c), warm (cool) colors indicate high (low) soil moisture values, opposite to the commonly used color scheme in hydrological studies.
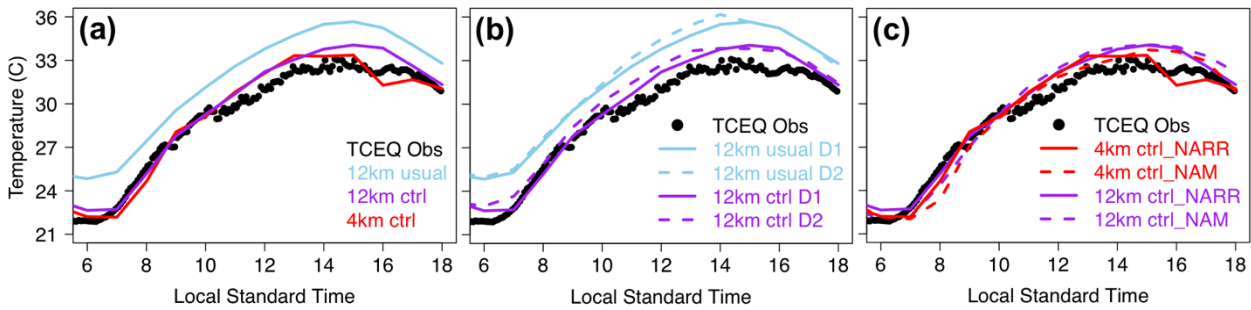
Figure 4: Comparing NUWRF daytime surface air temperature with the 5-minute TCEQ surface in-situ measurements (black dots) at Conroe, TX, on 11 September, 2013: (a) Evaluating the impact of NUWRF land initialization and grid resolution; (b) Evaluating the impact of NUWRF simulation length, including 1-day (D1) and 2-day (D2) forecasts, on the 12 km grid; (c) Evaluating the impact of NUWRF atmospheric initialization (using NARR and NAM) on 12 km and 4 km grids.
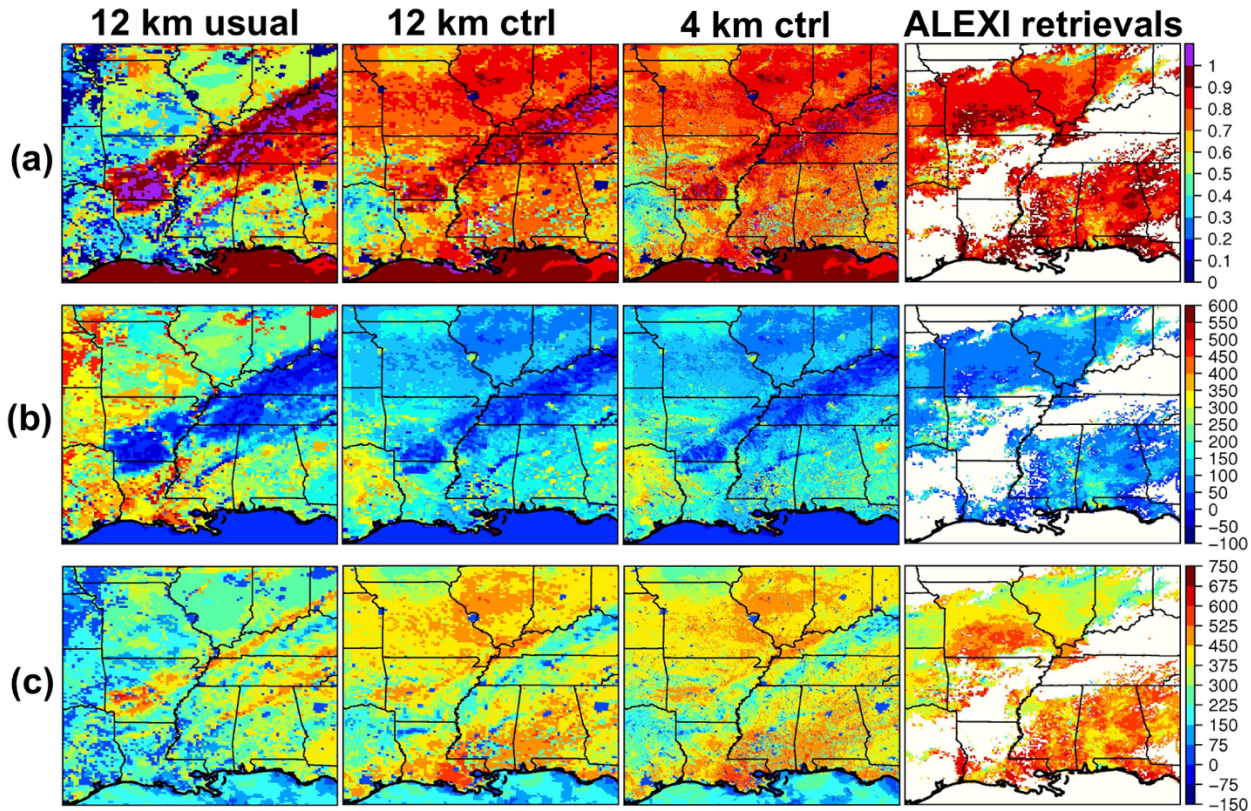

Figure 5: Comparing (a) evaporative ratio, unitless, defined as latent heat/(latent+sensible heat); (b) sensible heat in W/m^2, and (c) latent heat in W/m^2 from three NUWRF simulations (first three columns) with the NOAA operational 0.08°×0.08° ALEXI retrievals (right), on 11 September, 2013.
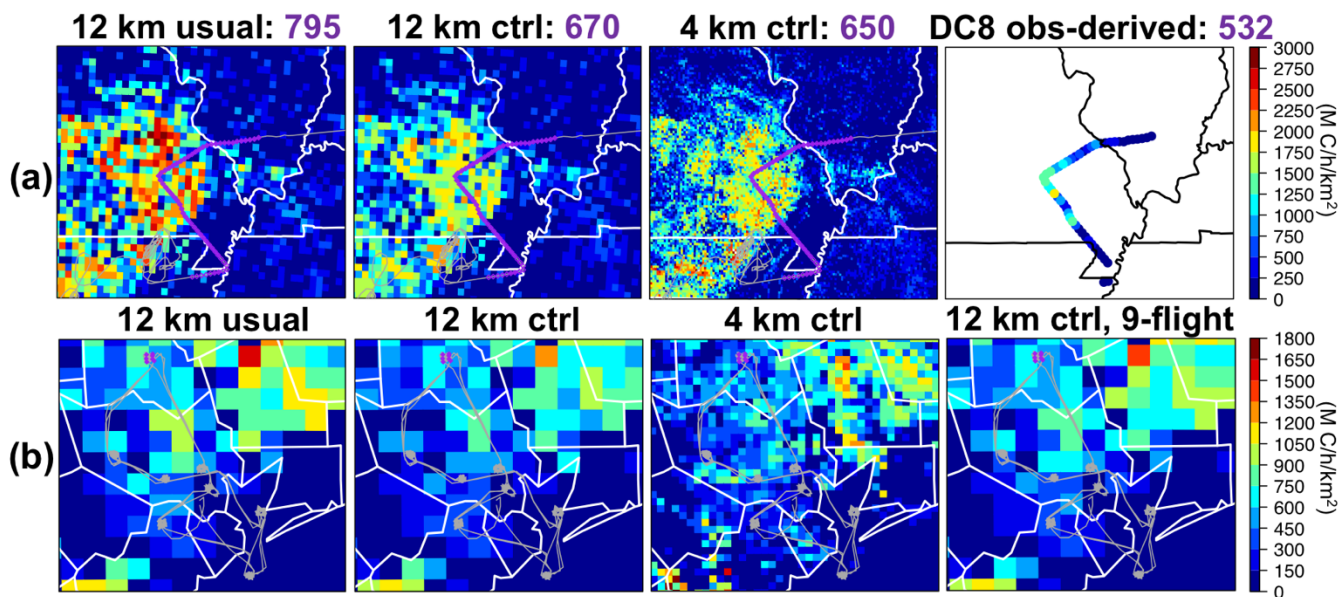
Figure 6: (a) Isoprene emissions around the "isoprene volcano" areas in Missouri based on NUWRF-MEGAN and aircraft observations at ~13 local standard time on 11 September, 2013. The mean values along the DC-8 flight path during 12:30-13:30 local standard time (in purple) are indicated in the figure captions. Open purple dots along the flight path refer to where isoprene data are missing or above the PBL. (b) Isoprene emissions in Houston, TX from NUWRF-MEGAN on 11 September, 2013 and on 9 DISCOVER-AQ flight days in September 2013, at local noontime. The DISCOVER-AQ P-3B flight path on 11 September, 2013 is overlaid in grey and the Conroe samples at around the noontime are highlighted in purple. Note that the flight paths for all other flight days are similar to but not exactly the same as that of 11 September.
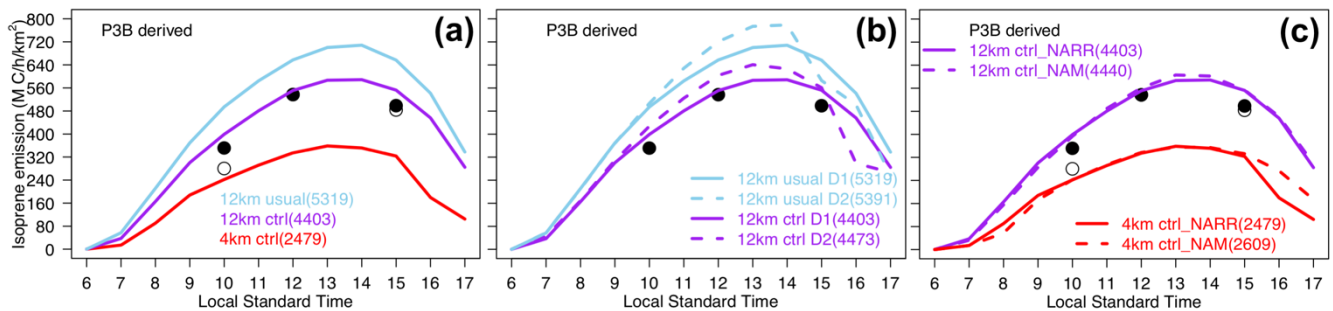
5

10

Figure 7: Comparing NUWRF-MEGAN daytime isoprene emissions in Conroe on 11 September, 2013 with the observation-derived emissions. The filled and open black circles indicate the calculations based on PBLHs from the 12 km and 4 km NARR IC/LBC ctrl runs, respectively: (a) Evaluating the impact of NUWRF land initialization and grid resolution; (b) Evaluating the impact of NUWRF simulation length, including 1-day and 2-day forecasts, on the 12 km grid; (c) Evaluating the impact of NUWRF atmospheric initialization (using NARR and NAM) on 12 km and 4 km grids. The daytime-integrated emissions are included in the parentheses, in MC/km^2.
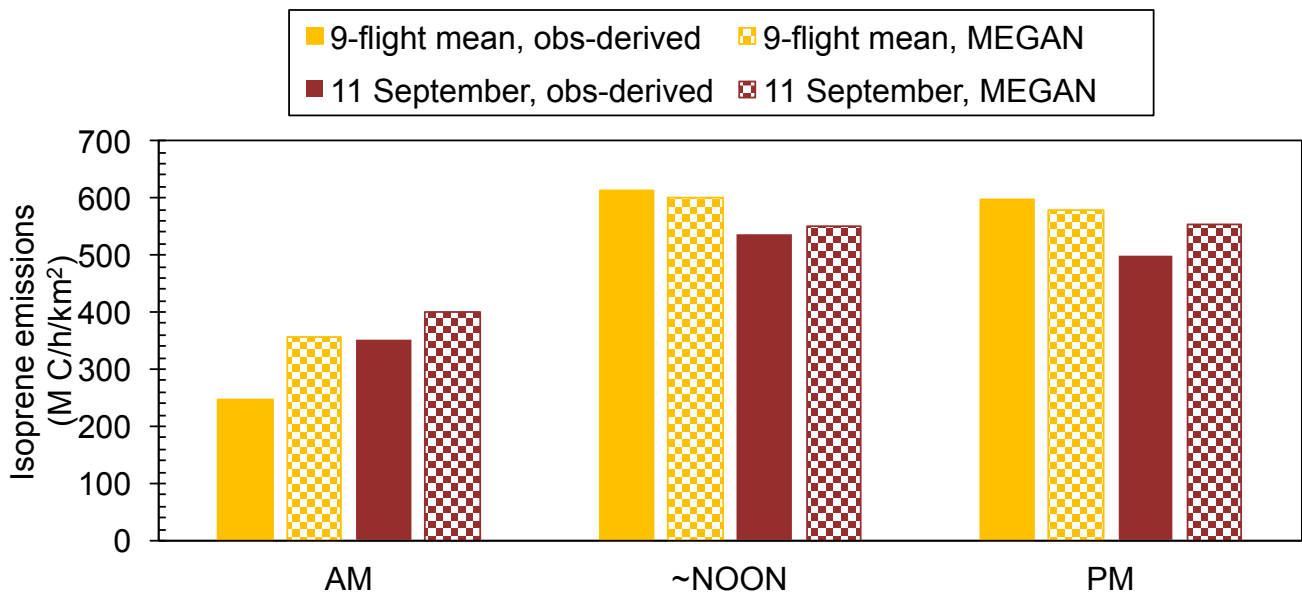

Figure 8: Temporal variability (AM: 15-16 UTC; ~noon: 18-19 UTC; PM: 20-21 UTC) of isoprene emissions in Conroe averaged on multiple DISCOVER-AQ flight days in September 2013 from NUWRF-MEGAN and aircraft observations, compared with the 11 September, 2013 conditions. The multi-flight day mean P-3B isoprene, NAQFC CMAQ OH and NUWRF PBLH were used to derive the multi-day mean observation-based emissions. The model data are from the 12 km NUWRF ctrl run.

35

Tables

Table 1: Summary of all NUWRF simulations in this study. More descriptions of these simulations can be found in Figure 1 and Section 2.1.3.

Case Name	Horizontal resolution	Land initialization	Atmospheric initialization/ Lateral boundary conditions	Approach illustrated in Figure 1
12 km usual(_NARR)[a]	12 km	NARR	NARR	(a)
12 km usual_veg(_NARR)[a,b]	12 km	NARR	NARR	(a)
12 km ctrl(_NARR)[a]	12 km	LIS	NARR	(b)
4 km ctrl(_NARR)[a]	4 km	LIS	NARR	(b)
12 km ctrl_NAM	12 km	LIS	NAM	(c)
4 km ctrl_NAM	4 km	LIS	NAM	(c)

5   [a]The *_NARR simulations are the focus of this study and the "(*_NARR)" part in the case names was often omitted in figures and texts. [b]Results are only shown in Figure S4 and briefly discussed in Section 3.1.1.

Table 2: NUWRF PBLH and air temperature performance along the DC-8 flight path (at where the isoprene data are available) around the Missouri "isoprene volcano" region on 11 September, 2013. A 1.6 km PBLH, which approximates to the 4 km/12 km simulated mean values (in italic/bold), was used to derive the emissions. Spatial distribution of the air temperature biases is shown in Figure S3.

Dataset	PBLH (km), mean ± standard deviation	Air temperature (°C), mean ± standard deviation	Air temperature RMSE (°C)
DC-8	1.454±0.308[a]	26.841±3.620	/
NUWRF 4 km ctrl	*1.551*±0.304	27.255±3.852	0.735
NUWRF 12 km ctrl	*1.569*±0.369	27.138±3.962	0.771
NUWRF 12 km usual	2.190±0.630	28.757±4.499	2.241

[a]Compared with the other used DC-8 datasets, the DIAL-HSRL dataset has different temporal resolution and completeness. Its mixed layer heights may be highly uncertain.

15

Table 3: NUWRF-simulated median PBLH (km) and daytime (6-17 local standard time) surface air temperature performance at different times of 11 September, 2013, at around Conroe, TX. The bold italic numbers were used to derive emissions.

NUWRF Case Name	PBLH (km)			Surface air temperature (°C)[a]	
	Morning	~Noon	Afternoon	Mean bias	RMSE
4 km ctrl	*0.666*	*1.467*	*1.752*	0.159	0.747
12 km ctrl	*0.839*	*1.465*	*2.038*	0.640	0.864
12 km usual	1.195	1.746	2.337	2.473	2.507

[a]The two data points nearest to 00:00 (minute:second) from the TCEQ 5-minute special ground observations were averaged and compared with the NUWRF output hourly-recorded at 00:00.